Photoelectron Spectra of Hot Polyatomic Ions: A Statistical Treatment of Phenide

Beverly Ru and Andrei Sanov*

Department of Chemistry and Biochemistry, The University of Arizona,

Tucson, Arizona 85721, United States

* Email: sanov@arizona.edu

KEYWORDS: Photoelectron imaging spectroscopy; Polyatomic ions; Phenide; Density of states

ABSTRACT

Many distinct vibrational states contribute to the congested photoelectron spectra of hot polyatomic anions. This often makes the complete Franck-Condon (FC) analysis both impractical and unnecessary. Although it is common to limit the FC calculations to a subset of the FC-active modes, such limited approach is strictly applicable to the ground-state (cold) anions only. At high temperatures, all vibrational modes participate in thermal excitation, and the FC and thermal activities become intertwined. We report the photoelectron spectra of ~700 K phenide ($C_6H_5^-$) obtained at 355 nm (3.49 eV), 532 nm (2.33 eV), and 611 nm (2.03 eV) and describe several practical models that help interpret and analyze the results. Among them are the active-modes model, the active modes + dark bath and the active modes + bright bath models, and finally, the energy-conservation model. The models combine the results of limited (and, therefore, feasible) FC calculations with statistical analysis and provide efficient means of determining the ion temperature from the broad and congested photoelectron spectra. The described capability can be applied to hot plasmas, the collisional excitation or cooling of ions, and evaporative cooling in cluster ions.

1. Introduction

The density of states of a polyatomic molecule (or ion) increases rapidly with excitation energy. This has a significant effect on the thermodynamic and spectroscopic properties of thermally excited ensembles.[1-3] The dense manifolds of vibrational states populated at higher temperatures may result in broad and congested absorption spectra consisting primarily of hot bands. The state-resolved modeling techniques commonly used for cold molecules may become impractical under these conditions, while the loss of state-dependent information in the averaged spectra diminishes the criticality of the state-specific calculations. Altogether, these considerations may call for a statistical rather than state-resolved approach to spectral modeling. Why, for example, calculate a myriad of state-specific Franck-Condon factors for a hot polyatomic, if the individual transitions are not resolved in the highly congested spectra anyway?

This work focuses on the photoelectron spectroscopy of hot phenide ($C_6H_5^-$, i.e., deprotonated benzene) as an example of a moderately-sized polyatomic ion. The 27 vibrational modes of phenide (Ph^-) yield 26 distinct vibrational states below 0.135 eV, and 2171 states below 0.350 eV. These state counts stand in sharp contrast with any diatomic species. For example, O_2^- has only 1 and 2 vibrational states, respectively, under the above limits. These arbitrary thresholds may seem high (in terms of kT, they correspond to 1570 and 4060 Kelvin), but the canonical temperature of Ph^- does not need to be close to those values for the corresponding levels to contribute significantly to the vibrational partition function.

At thermodynamic equilibrium, the population of each quantum state is proportional to the Boltzmann factor, while the energy distribution is given by:

$$P(E) = cg(E)e^{-E/kT}, \tag{1}$$

where E is excitation energy, $g(E)$ is the density of states (DOS), k is the Boltzmann constant, T is absolute temperature, and c is a normalization constant. In the classical harmonic limit[1,4] the vibrational DOS of a polyatomic molecule scales as $g(E) \propto E^{n^*-1}$, where n^* is the effective number of active oscillators satisfying the classical requirement $h\nu_i \ll E$. Here, ν_i, i = 1, …, ($3N$ – 6), are the fundamental normal-mode frequencies, with N being the number of atoms in the polyatomic molecule or ion. Since the number of active modes increases with E, n^* itself increases with energy, approaching the ($3N$ – 6) limit only at very high temperatures.

Yet even at moderate temperatures, where the classical condition is not satisfied, a rapidly

rising $g(E)$ in Eq. 1 can shift the population maximum, as well as $\langle E \rangle$, to many folds of kT. Therefore, a realistic approach to modeling the spectra of high-temperature polyatomics must account for a multitude of thermally excited states, leading to a potential bottleneck in state-specific calculations. For example, a Franck-Condon (FC) analysis[5-7] accounting for all vibrational states that contribute significantly to the partition function of phenide at $T \sim 1000$ K would take millennia of computing time (*vide infra*). In contrast, similar calculations in the oft-assumed 0-300 K range require few initial states to be considered and thus avoid the above limitation.[8-12]

Elevated temperatures come into play in many important environments, including planetary and stellar atmospheres, hot plasmas, combustion reactions, to name just a few. Hence, this spectroscopic regime is important to consider. We first encountered it inadvertently, after modifying our anion source[13-15] with the goal of increasing the ion density. The change (described in Section 2) resulted in warmer ions and prompted us to seek an efficient method for quantifying their temperature based on the observed spectra. This article describes our initial findings for Ph^-.

To set the stage, Figure 1 compares the statistical properties of Ph^- and O_2^- over the temperature range of 0–1000 K, with NO_2^- also included as an intermediate case. All ions were treated in the harmonic approximation. The O_2^- and NO_2^- properties were evaluated via a direct state count, using the vibrational frequency of 1090 cm^{-1} for the former[16-17] and the 1268, 776, and 1242 cm^{-1} normal-mode frequencies for the latter.[18-19] The corresponding details for phenide are given in Section 6.2. Figure 1a shows the temperature-dependent population fractions of the ground vibrational state (v = 0) and the combined fractional populations of the ground and singly excited states (labeled as v = 0, 1). Single excitations were chosen because they (and only they) are often included by default in FC simulations of photoelectron spectra. For O_2^-, the v = 0, 1 curve represents the two lowest vibrational states. For NO_2^-, it represents the combined populations of four states: the ground state plus the three singly excited normal-mode vibrations. For Ph^-, the v = 0, 1 curve corresponds to 28 states: the ground state plus the fundamental excitations of the 27 normal modes.

The difference between the diatomic and polyatomic populations is striking. While the fast majority (≥ 80%) of O_2^- is in the ground state at any temperature in the analyzed range, most of the Ph^- ions are vibrationally excited already just above the room temperature, at $T > 307$ K. At $T > 430$ K most of Ph^- is excited beyond single excitations. These results suggest that any model

of phenide without hot bands is inadequate for $T > 300$ K. For $T \gtrsim 400$ K not only single, but double and higher-order excitations and combination bands must be included. Shaded in Figure 1 is the 300-700 K temperature range, within which the role of the ground vibrational state of Ph^- changes drastically: from the dominant 52% (300 K) to the nearly inconsequential 1.5% (700 K).

A different way of illuminating the role of thermal excitations in polyatomic spectra is presented in Figure 1b. Here we show the temperature dependence of the average vibrational energy of Ph^-, with NO_2^- and O_2^- included again, for comparison. If n^* is the effective number of active vibrations, $\langle E \rangle = n^* kT$ is expected. At $T < 300$ K, Ph^- can be described as cold, with n^* increasing from 0.055 at 100 K to 1.8 at 300 K. This is still small compared to the number of the anion's vibrational modes (27). At higher T, the vibrations play a more prominent role. Already at 500 K, $\langle E \rangle$ of Ph^- is 0.2 eV, corresponding to $n^* = 4.7$ units of kT, while at 700 K, it reaches $7.1kT$.

The model approaches described in this work can be applied to any polyatomic species, but phenide proved to be an ideal system due to its just-right size. As seen in Figure 1a, the population distribution of phenide undergoes a rapid change in the 300-700 K range. The lower bound of this range is the temperature assumed in most published FC calculations, including but not limited to those for phenide,[20-21] while the upper bound corresponds to our modified ion source.

Phenide photodetachment yields the phenyl radical (Ph). Ph is an important intermediate in the formation of polycyclic aromatic hydrocarbons.[21-24] It is involved in many notable reactions, from interstellar space[22-28] to combustion chemistry, including the formation of soot.[29-30] Photoelectron spectroscopy of Ph^- at ~300 K was previously studied by Lineberger and co-workers.[20] The ~700 K photoelectron spectra obtained in our work are significantly different, for the statistical reasons highlighted in Figure 1, and hence we aim to establish a connection between the observed spectral envelopes and the canonical temperature of the ions.

The experimental methodology and the results of the experiments on hot Ph^- are described in Sections 2 and 3, respectively. Section 4 presents the results of quantum chemical calculations on the anion and two lowest electronic states of the neutral radical, yielding their equilibrium geometries and vibrational frequencies. In Section 5, the FC calculations for the cold and hot phenide ions are reported, within the limitations set by the computing times. In Section 6, the results of the limited FC calculations are combined with statistical approaches under various assumptions about the couplings between the FC-active and inactive vibrational modes. A summary of the results and the overall conclusions are presented in Section 7.

2. Experimental Methods

The negative-ion photoelectron imaging spectrometer used in this study has been described elsewhere.[31-32] Here we highlight the modified ion source, which is illustrated schematically in Figure 2. Instead of a conventional electron gun,[13] this source configuration uses its stripped-down version, which we refer to as the electron cannon.[33]

Benzeneselenol (PhSeH), also known as selenophenol, was used as the precursor to produce the Ph^- anions. Argon gas at a backing pressure of 1.8 atm was passed through a sealed container with the liquid precursor (1 torr vapor pressure) kept at room temperature. The resulting gas mixture was expanded into the high-vacuum source chamber ($2\times10^{-7}/5\times10^{-5}$ torr base/operational pressure) through a pulsed supersonic nozzle (General Valve, Inc., Series 9, 0.8 mm diameter orifice). The nozzle was operated at a repetition rate of 20 or 50 Hz, matching that of the laser used in each measurement.

The electron cannon is positioned next to the nozzle, opposite the Faraday cup, as shown in Figure 2. It consists of a ~1 mm wide thoria-coated iridium ribbon filament (e-Filaments, LLC) and an anode. Both the filament and the anode are floated at −100 to −150 V, with an additional small negative potential optionally applied to the anode. The filament is heated by a 4-5 A direct current from a floated supply and emits electrons via a thermionic process. The electrons from the filament's tip protruding slightly through a 4 mm diameter orifice in the anode, create a wide cone of bombardment of the supersonic expansion, producing an electron-impact ionized plasma. Compared to a typical electron gun, the cannon, stripped of the focusing and steering elements, offers less precision, but requires less optimization and results in an increased ion signal. Critically, the unfocused spray of 100-150 eV electrons ionizes a large volume of the expansion, with the bombardment occurring, on average, many nozzle diameters downstream from the expansion origin. The resulting ions experience little collisional cooling since it is most effective within the first few nozzle diameters from the nozzle. The ions therefore have significantly higher internal temperatures compared to a traditional ion source using a collimated electron beam.[13,31]

Next, the anions are separated according to their masses in a Wiley-McLaren[34] time-of-flight mass-spectrometer.[31-32] The Ph^- packets are intersected in space and time by a pulsed laser beam to photoeject electrons. The 532 nm and 355 nm light pulses were produced as a second and third harmonics, respectively, of a Spectra Physics Lab-130-50 Nd:YAG laser (50 Hz repetition rate). 611 nm light was produced by a Rhodamine 640 dye in an ND6000 dye laser pumped by the

second harmonic of the Surelite II-20 Nd:YAG laser (Continuum, Inc., 20 Hz repetition rate).

The photodetached electrons are projected onto a 40 mm diameter position-sensitive dual microchannel plate imaging detector coupled to a P47 phosphor screen by using a velocity-map[35] imaging[36-37] assembly.[31] The resulting photoelectron images, fiber-optically projected on an outside window, are captured using a charge-coupled device camera (Roper Scientific, Inc.). All images reported here correspond to multiple runs, totaling $\sim 10^6$ experimental cycles per image. The photoelectron spectra were obtained from the images via an inverse Abel transformation[37] using the BASEX program from Reisler and co-workers.[38]

3. Experimental Results

An overview of the experimental results is presented in Figure 3. The photoelectron images of Ph^- were recorded at (a) 355 nm (3.49 eV), (b) 532 nm (2.33 eV), and (c) 611 nm (2.03 eV). The raw images and corresponding photoelectron spectra are shown separately for each wavelength. The experimental spectra are compared to the model spectra for cold phenide (light blue), obtained as described in Section 5.2. All spectra are plotted with respect to electron binding energy (eBE), defined as the difference between the photon energy ($h\nu$) and the measured electron kinetic energy (eKE). Due to the conservation of energy, eBE = $h\nu$ – eKE equals the energy gap between the target neutral and the initial anion states.

The 532 nm (2.33 eV) and 611 nm (2.03 eV) photoelectron spectra in Figure 3b-c each consist of a single broad band (X), corresponding to the ground electronic state of the phenyl radical. The 355 nm (3.49 eV) spectrum in Figure 3a additionally includes the first excited state of phenyl (A). The model peaks marked with stars in Figure 3 are the corresponding transition origins and all experimental signal to the left of them is due to hot bands. This is a clear and immediate indication of the high temperature of the ions in this experiment.

The laser polarization direction is vertical in the plane of all images in Figure 3. We note the clearly parallel character of the X band photoelectron angular distribution (PAD) and the approximately isotropic nature of the A band. These PADs are consistent with the in-plane (σ) and out-of-plane (π) characters of the respective detachment orbitals.[39-40]

4. Geometric, Electronic, and Vibrational Structures

The phenide anion has a closed-shell electron configuration corresponding to the X^1A_1 electronic

state. Figure 4 shows the anion's canonical a_1 HOMO (highest-occupied molecular orbital) and b_1 HOMO−1. The orbitals have σ and π characters, respectively, consistent with the PADs noted in Section 3. Hence, electron detachment from the HOMO (X band) yields a σ radical (σ-Ph), i.e., phenyl in the ground electronic state, X^2A_1, while detachment from the HOMO−1 (A band in Figure 3a) produces a π radical (π-Ph), i.e., phenyl in its first excited electronic state, A^2B_1.

Due to the in- and out-of-plane characters of the HOMO and HOMO−1, a greater geometry change is expected for the $X^2A_1 \leftarrow X^1A_1$ transition (X band), compared to $A^2B_1 \leftarrow X^1A_1$ (A band). The sp^2 character of the deprotonated carbon's (C1) dominant contribution to the HOMO causes an increase in the C2-C1-C6 bond angle for the X transition (atom numbering is defined in Figure 5), leading to symmetry-preserving ring distortions.[20] In contrast, detachment from the π-character HOMO−1 has a minimal effect on the bond angles. Due to the C1-C2, C1-C6, C3-C4, and C4-C5 bonding and the C2-C3 and C4-C5 antibonding properties of the orbital, some lengthening of the first group of bonds and shortening of the latter is expected in the A band.

These qualitative predictions are confirmed by the geometry optimizations described next. The subsequent spectral analysis requires a reasonable description of the anion and neutral vibrational structures, but high precision of the mode frequencies is not necessary since the details are washed out in the averaged spectra. The harmonic approximation itself is expected to be a greater source of errors. For this reason, we limit the geometry optimizations and frequency calculations to the economical methods appropriate for each electronic state involved.

All electronic structure calculations were carried out using Q-Chem 5.1.[41] The aug-cc-pVDZ basis set was used throughout. The Ph^- and σ-Ph geometries were optimized using the B3LYP density functional and the results are presented in Figure 5a and Table 1. Since the anion and neutral structures are similar, and both are of C_{2v} symmetry, a single molecular frame is shown in the figure for the anion and the neutral. The geometric parameters on the left side correspond to the anion, on the right—the neutral σ radical. Only few key parameters are included in the figure, but the complete sets are given in Table 1. The 27 vibrational frequencies of Ph^- and σ-Ph, as well as the corresponding normal mode symmetry species, are summarized in Table 2. To be consistent with the previous work on phenide,[20-21] we follow the standard Mulliken notation for all electronic and vibrational symmetry labels. Under this convention, the π HOMO−1 shown in Figure 4 transforms under the B_1 irreducible representation (B_1 and B_2 are flipped in Q-Chem).

The excited electronic state of phenyl, π-Ph, was characterized using the equation-of-motion (EOM) ionization-potential (IP) method[42] combined with the coupled-cluster theory with single and double excitations (CCSD). The target state was accessed by removing an electron from the b_1 HOMO−1 of the closed-shell anion CCSD reference. The potential gradient was followed to yield the π-Ph equilibrium geometry and vibrational normal modes. The optimized parameters are given in Table 1, while the mode frequencies and symmetries are summarized in Table 2. A comparison of the Ph^- and π-Ph equilibrium structures is given in Figure 5b. To avoid comparing structures from different methods, the Ph^- geometry was additionally optimized using CCSD (Table 1) and it is these results that are shown on the left side of Figure 5b.

In accordance with the spectroscopic convention, E' will be used to denote the vibrational energy of neutral phenyl (the target state), while E'' (or E) is reserved for the vibrational energy of the anion (the initial state). Similarly, i' and i'' = 1–27 will be used to index the target (Ph) and initial (Ph^-) vibrational modes, respectively, in the order of ascending frequencies. These indices appear in the first column of Table 2. The frequencies and the modes themselves are denoted ν_i' and ν_i'', where $i = i'$ or i'', as appropriate. The number of excitation quanta in each mode is n_i' or n_i''. In general, the anion and neutral normal modes are not identical, and even similar modes do not necessarily follow the same frequency order. Several modes of Ph^-, σ-Ph, and π-Ph, to which special attention will be paid in the following analysis, are depicted in Figure 6 and highlighted/ bolded in Table 2. As a case in point, the ν_4' mode of σ-Ph corresponds closely to ν_3'' of Ph^-.

5. Franck-Condon Simulations

5.1. General details. The FC simulations relied on the overlap integrals (FC factors) calculated using ezFCF, part of the ezSpectra suite of programs developed by Gozem and Krylov.[43] The harmonic frequencies of Ph^-, σ-Ph, and π-Ph from Table 2 and the corresponding normal-mode coordinates were used as inputs. The FC factors for all reported results were obtained in the parallel-mode approximation, but in several cases very similar spectra were calculated (as a check) using the Duschinsky rotations of the normal modes.[44] Table 3 provides a summary of the key FC calculations, either completed or attempted, listing the normal modes included, the excitation limits used, as well as the approximate or estimated computing times.

To generate model spectra for comparison with the experiment, the transition intensities, i.e., the FC factors squared, were multiplied by the corresponding Boltzmann factors, $e^{-E''/kT}$, and

scaled by a Wigner-like[45] function $f_w(\mathrm{eKE}) = \mathrm{eKE}^P$ to account for the electronic cross-section's eKE-dependence,[46-50] with P = 1/2 used throughout. Although this value strictly corresponds to zero-dipole *s* wave emission only, it is expected to perform well for the relatively small dipole moment of phenyl (0.87 Debye for σ-Ph, based on B3LYP). Inclusion of $f_w(\mathrm{eKE})$ is especially important for the small-eKE parts of band X at 532 and 611 nm, as well as the entire A band at 355 nm (Figure 3). The Wigner-scaled FC stick spectra were convoluted with a Gaussian function to account for the experimental broadening. In all comparisons with the imaging measurements (performed in the velocity domain), the broadening width was assumed to be eKE-dependent, mimicking the experimental resolution. The full width at half-maximum was defined as $w_0\sqrt{\mathrm{eKE}}$, where w_0 was chosen to be about 0.02 $\mathrm{eV}^{1/2}$, depending slightly on the measurement.

5.2. The cold phenide spectrum. An overview of the FC simulations of the σ-Ph (band X) transition in cold Ph^- is shown in Figure 7. The most complete model spectrum is shown in Figure 7a (light blue). To check its quality, it is compared with the vibrationally resolved 351 nm (3.53 eV) experimental spectrum obtained by Lineberger and co-workers at ~300 K.[20]

The model spectrum in Figure 7a was obtained using the FC factors from run X3 (Table 3), which included all 27 vibrational modes of σ-Ph. The number of excitation quanta in the target state was limited to $\max(\sum n_i') = 10$. No excitations were permitted in the anion (all $n_i'' = 0$), limiting the applicability of this calculation to cold ions only. The Wigner-like scaling was defined by Lineberger's 3.53 eV photon energy, while the width of the broadening function was set to 0.01 eV, matching the peak widths in the experimental spectrum.

The selection rules for photodetachment transitions require the initial and target vibrational states to have the same symmetry. Since the ground state is totally symmetric, only A_1 symmetry neutral states can be accessed in cold-ion photodetachment. With this in mind, we performed another FC calculation with only the A_1 symmetry modes, of which there are 10 (Table 2). With the smaller number of modes included in run X4 (Table 3), the maximum number of excitations in the target state was increased to 16. Any state that includes A_1 excitations only satisfies the A_1 symmetry requirement, but not all A_1 states are exclusive to the A_1 modes. For example, given the A_2 symmetry of ν_1' (Table 2), the $2\nu_1'$ state has the A_1 symmetry ($A_2 \otimes A_2 = A_1$), though the mode itself does not. Although restricting the FC calculation to the A_1 modes does not account for all allowed target states, the model spectrum obtained from run X4 (not shown) is very similar to the one from run X3 (Figure 7a). We draw two conclusions from this observation. First, the

A_1 modes are indeed nearly entirely responsible for the cold spectrum. Second, the limit of 10 vibrational quanta in the target state is sufficient at $T = 0$. (Decreasing it below 10 leads to a noticeable truncation of the high-eBE tail of the model spectrum.)

We will use the run-X3 FC factors for comparison with hot-ion data. Figure 3 and subsequent statistical analysis figures include the $T = 0$ K reference spectra (in light blue). These were calculated using the same FC factors as the blue spectrum in Figure 7a but were Wigner-corrected for the appropriate laser wavelength in each case. The lowest-eBE peaks marked with stars in Figure 3 are the X band's origin (eBE = 1.096 eV), which corresponds to the adiabatic electron affinity (EA) of σ-Ph.[20] For comparison, the B3LYP calculations in Section 4 predict an EA of 1.039 eV. As already mentioned, all spectral intensity to the left of these peaks is due to hot bands.

Moving on to band A in Figure 3a, the 3.49 eV energy of a 355 nm photon exceeds the adiabatic attachment energy (electron affinity) of π-Ph, EA(π) = 3.439(6) eV, by only 0.05 eV. This difference, which corresponds to ~400 cm^{-1}, is smaller than the lowest A_1 symmetry vibrational frequency in π-Ph (Table 2). Therefore, only the 0-0 vibrational transition within the A band is accessible in cold Ph^- at 355 nm. The above value EA(π) is calculated by combining the high-precision 2.343 eV term energy of the $A\,^2B_1$ state of phenyl[51-52] with the EA of σ-Ph, 1.096(6) eV.[20] For comparison, the EOM-IP-CCSD calculations in Section 4 predicted a vertical attachment energy of 3.136 eV for the π-Ph equilibrium. Unlike its adiabatic counterpart, the vertical value does not account for the anion geometry relaxation and is therefore smaller than EA(π).

Figure 8 compares the A band stick spectrum (FC factors squared, uncorrected for the Wigner scaling and hence extending beyond the photon energy) to the experimental band expanded from Figure 3a. The FC factors are from run A1 (Table 3), which included all vibrational modes of the neutral, but allowed no excitations in the anion ($T = 0$). The corresponding Wigner-corrected and broadened spectrum consists of a single peak at the transition's origin ('o' in Figure 8). It is shown in light blue in Figure 3a and several subsequent figures. The relative normalization of the simulated A and X band intensities is arbitrary.

It is important to understand why Lineberger's 351 nm (3.53 eV) spectrum includes only a hint of band A,[20] while in ours ($h\nu = 3.49$ eV) this band is as intense as X (Figure 3a). First, as mentioned in their report, Lineberger's apparatus has diminishing sensitivity to low-eKE electrons, while our imaging analyzer is equally sensitive at any eKE, up to the limit set by the detector radius. Second, the temperature of the ions is higher in our experiment and most of our

A band's intensity in Figure 3a is attributed to hot bands.

5.3. Active modes. The past studies[20-21] additionally demonstrate that band X in cold phenide is dominated by just two σ-Ph modes. Lineberger and co-workers attributed the band structure to the 600(10) and 968(15) cm^{-1} vibrations.[20] They gave a definitive assignment for the first mode, ν_4' in our notation. They also identified two candidates for the second vibration, corresponding to our ν_{10}' and ν_{12}' (Figure 6), but the data were insufficient to discriminate between the two. Our ezFCF runs X3 and X4 identify ν_4' and ν_{10}' as primarily responsible for the structure of band X, confirming a similar conclusion of Sivaranjana Reddy et al.[21] Both modes are symmetric ring distortions, consistent with the geometry difference between Ph^- and σ-Ph (Figure 5a).

Hence, it is tempting to limit the modeling of band X to just the ν_4' and ν_{10}' normal modes of σ-Ph. The result of the $\{\nu_4', \nu_{10}'\}$ approach (run X6) at T = 0 K is shown in Figure 7b (purple). While the band structure is well reproduced, the intensity of the higher-eBE shoulder is underestimated compared to both the experimental spectrum (also included in Figure 7b) and the full FC simulation (blue in Figure 7a). The shoulder is significantly improved if the ν_{12}' mode is added to the calculation. This mode was the second candidate suggested by Lineberger and co-workers for the higher-frequency progression.[20] The $\{\nu_4', \nu_{10}', \nu_{12}'\}$ cold-ion spectrum is shown as a green trace in Figure 7b. It is based on the FC factors determined from run X5 (Table 3), with T = 0 K. While the $\{\nu_4', \nu_{10}', \nu_{12}'\}$ simulation is more successful, compared to $\{\nu_4', \nu_{10}'\}$, in describing the band's right shoulder, it still falls noticeably short of the all-modes calculation in Figure 7a.

There is another reason to include ν_{12}' in the vibrational space used in the following statistical analysis. Our model simulations rely on the relative mappings of the neutral and anion vibrations. As seen in Figure 6, the first FC-active mode of σ-Ph, ν_4', corresponds closely to the ν_3'' mode of the anion, but ν_{10}' does not map adequately on any one anion mode. Instead, it is best described as a superposition of two modes, ν_{10}'' and ν_{12}''. Similarly, ν_{12}' is also best viewed as a superposition of ν_{10}'' and ν_{12}''. Thus, representing the coordinates of the two σ-Ph modes which dominate the cold Ph^- spectrum requires three modes of the anion, ν_3'', ν_{10}'', and ν_{12}''. Preserving the dimensionality, we define the FC-active vibrational space in terms of either three neutral modes, ν_4', ν_{10}', and ν_{12}', or the corresponding three anion modes, ν_3'', ν_{10}'', and ν_{12}''. These two spaces are approximately the same, and we will view them as one. To be succinct, this FC-active space will be denoted $\mathbf{Q}_X^3 \equiv \{\nu_3'', \nu_{10}'', \nu_{12}''\} \approx \{\nu_4', \nu_{10}', \nu_{12}'\}$, where superscript 3 is the space's dimensionality, while subscript X refers to the X band.

The A band spectrum (Figure 8) similarly shows three dominant π-Ph modes excited in the photodetachment: ν_4', ν_9', and ν_{22}'. Based on the mode representations in Figure 6, these modes overlap closely with the respective ν_3'', ν_{10}'', and ν_{21}'' normal modes of the anion. Therefore, the FC-active space for the A band is defined as $\mathbf{Q}_{\mathrm{A}}^3 \equiv \{\nu_3'', \nu_{10}'', \nu_{21}''\} \approx \{\nu_4', \nu_9', \nu_{22}'\}$.

5.4. Isolated active modes in hot ions. At higher temperatures, a full FC calculation, analogous to the simulation in Figure 7a but including not only the neutral but also the anion excitations up to an adequate limit, would take millennia to complete (X1 and X2 in Table 3). In search of a different approach, we will limit the FC calculations to the $\mathbf{Q}_{\mathrm{X}}^3$ and $\mathbf{Q}_{\mathrm{A}}^3$ spaces defined in Section 5.3 and then, in Section 6, use statistical modeling to account for all other vibrations. The X band FC factors for $n', n'' \in \mathbf{Q}_{\mathrm{X}}^3$, with $\max(\sum n_i') = \max(\sum n_i'') = 24$, were calculated in Section 5.3 (ezFCF run X5). Using these factors, Figure 7c shows the effect of increasing the $\mathbf{Q}_{\mathrm{X}}^3$ temperature from 0 to 1000 K.

For detailed modeling of the hot-ion spectra, we first turn to the A band. Unlike X, it shows a partially resolved vibrational structure in the experimental spectrum in Figure 3a. Moreover, this band's 355 nm (3.49 eV) model spectrum at T = 0 K consists of only the origin peak ('o' in Figure 8), represented by the lone light-blue peak at eBE = 3.439 eV in Figure 9a and b.

The A band FC factors for $n', n'' \in \mathbf{Q}_{\mathrm{A}}^3$, with $\max(\sum n_i') = \max(\sum n_i'') = 24$, were calculated in run A2 (Table 3). The dark blue and red model spectra in Figure 9a correspond to $\mathbf{Q}_{\mathrm{A}}^3$ temperatures of 3400 and 6000 K, respectively. They are compared to the experimental spectrum from Figure 3a. The vibrational structure in the model spectra agrees with the discernable experimental peaks. Each model peak labeled in the figure consists of multiple overlapping transitions; their aggregate assignments are given in the inset in terms of the changes in the ν_3'' and ν_{10}'' excitations upon photodetachment. (Mode ν_{21}'' also contributes, but less than the other two.) For example, peak 'a' corresponds to the loss of one ν_3'' excitation and the gain of one in ν_{10}''.

In estimating the temperature, we focus on the low-eBE part of the spectrum, which is due exclusively to the thermally excited ions. The T = 3400 K spectrum in Figure 9a gives the best overall agreement with the experiment, but overestimates the relative intensity of the origin peak. This discrepancy is addressed in Section 6.3. The 6000 K red trace is shown in Figure 9a to confirm that these simulations allow for sufficient vibrational excitations in the anion and the neutral. To stress this point, Figure 9b shows the corresponding results obtained with $\max(\sum n_i') = \max(\sum n_i'') = 8$ (run A3 in Table 3), instead of 24 in Figure 9a. Not only reducing the excita-

tion limits yields colder-looking spectra, but there is less difference between the 3400 K and 6000 K simulations in Figure 9b. This is because the band includes many transitions from thermally excited anions with more than 8 quanta distributed among the active modes.

A similar approach was used to simulate the X band transitions at all wavelengths studied. The results are shown in Figure 10 (red), in comparison with the experimental spectra (black). Similar to Figure 3, shown in light blue are the all-modes FC spectra of cold phenide, Wigner-adjusted for the corresponding wavelengths. The A band simulation at 3400 K in Figure 10a is reproduced from Figure 9a (blue). The temperature parameter in Figure 10a was adjusted independently for each band, to match the experimental spectrum in the respective low-eBE regions. It is encouraging that both X and A bands in Figure 10a are described by the same temperature. Still, the X band simulations in Figure 10 show discrepancies between the $\mathbf{Q}_{\mathrm{X}}^{3}$ model and the experiment on the higher-eBE side. These discrepancies are attributed to the unphysical exclusion of the FC-inactive modes, which do participate in thermal excitation. The low-eBE shoulders in the 532 and 611 nm spectra are best described with a slightly lower temperature of 3000 K, compared to 3400 K at 355 nm. This too is likely due to the model assumptions.

6. Statistical Approach to Hot-Ion Spectra

6.1. The need for a statistical approach. At cold temperatures, there is no need to consider vibrational excitations in the initial (anion) state. This simplifies the FC analysis, because only the FC-active modes must be considered in the neutral state. At higher temperatures, one must additionally contend with the thermal activity.

Thermal excitations are not subject to the Franck-Condon principle or spectroscopic selection rules: all vibrations are thermally active at sufficiently high temperatures. In the classical high-temperature limit, all 27 modes of Ph^- will be excited, each carrying, on average, one unit of kT. Even at moderate temperatures, just high enough for most population to be in excited levels ($T \gtrsim$ 300 K for Ph^-, according to Figure 1a), there is no physical justification for limiting the thermal excitation to a subset of modes. Since electrons can be detached from anions in any vibrational state, the thermal and FC activities become therefore intertwined.

Each vibrational state of the anion, $n'' = \{n_i''\}$, i = 1-27, possesses its own FC fingerprint, $F_{n''}$, which depends parametrically on n'' and has the explicit form of an FC factor (FCF) array defined in the space of all neutral states, $n' = \{n_i'\}$: $F_{n''}(n') = \mathrm{FCF}(n', n'')$. As already stated,

calculating the unique $F_{n''}(n')$, n', $n'' \in \mathbf{Q^{27}}$ (the complete space), arrays for all anion states with sufficient excitation limits would require millennia of computing time. Even if such impractical amount of effort could, hypothetically, be afforded, this approach would still be misguided. First, harmonic calculations that neglect couplings between the zeroth-order states are likely to be untrustworthy for highly excited levels. Second, the unique FC fingerprints of the individual anion states are anyway washed out in the congested spectra, making the cumbersome calculation of all individual FC factors quite unnecessary. Hence, in the following, we focus on the limited vibrational spaces spanned by the FC-active modes, defined in Section 5.3, and develop a statistical approach to account for the FC-inactive (but thermally active) vibrations.

6.2. The density of states and vibrational energy distribution of Ph^-. Given the dense manifold of excited states associated with the 27 vibrational modes, excited states of Ph^- can contribute significantly to the vibrational partition function at high temperatures. To stress this point, Figure 11 shows the vibrational energy distributions, $P(E)$, for Ph^- at various temperatures from 300 K to 1000 K. The distributions were calculated according to Eq. 1, using the DOS function $g(E)$ evaluated under the harmonic approximation. A direct state count in MATLAB using the fundamental mode frequencies of Ph^- from Table 2 was used in the E = 0–0.7 eV interval. This energy range was divided into 100 bins, and the state count for each bin was converted to the discrete DOS values by dividing it by the bin width. The binned $P(E)$ values are shown in Figures 11a-d by filled symbols.

Overall, 439,775 Ph^- states were identified below 0.7 eV (30 min of computing time). Above 0.7 eV, the direct-count approach rapidly becomes prohibitively time-consuming, so the $g(E) \propto E^{n^*-1}$ extrapolation was used instead. The proportionality coefficient and n^* were determined by requiring the continuity of $g(E)$ and its derivative at the E = 0.7 eV stitching point. The resulting extrapolations (with n^* = 9.5) are shown by red curves in Figures 11a-d. These and other similarly obtained distributions were also used to generate the plots in Figure 1. Since the effective number of oscillators is a monotonically increasing function of energy, all curves in Figure 11, obtained with the n^* values determined at the stitching points, underestimate the DOS—and, therefore, $P(E)$—at higher energies.

From these calculations, we conclude that at T > 700 K (kT > 0.06 eV), vibrational states with E > 1 eV contribute significantly to the partition function. To account for this polyatomic DOS effect, the upper bound of the anion excitation energy was set to 2.5 eV in all model calcu-

lations presented below. Even though this limit is above the adiabatic detachment threshold (EA = 1.096 eV),[20] the autodetachment rate at $T \sim 700$ K is expected to be low (and, in fact, not observed in the photoelectron images in Figure 3). Vibrational autodetachment requires more than EA of energy to be channeled in the electronic degrees of freedom, which is statistically unlikely due to the thermal excitation energy being partitioned amongst many vibrations.[53-58]

6.3. The dark-bath model. We will now assume that the FC-active modes are in thermodynamic equilibrium with the rest of the vibrations. For each of the X and A electronic transitions, we define the corresponding "bath" space, spanned by the coordinates of the 24 FC-inactive modes. For the X band, bath $\mathbf{B}_{\mathrm{X}}^{24}$ is obtained by excluding ν_3'', ν_{10}'', and ν_{12}'' from the complete set of Ph^- normal modes. For the A band, $\mathbf{B}_{\mathrm{A}}^{24}$ is obtained by similarly excluding ν_3'', ν_{10}'', and ν_{21}''.

The DOS functions for the bath spaces, $g_{\mathbf{B}_{\mathrm{X}}^{24}}(E_b)$ and $g_{\mathbf{B}_{\mathrm{A}}^{24}}(E_b)$, where E_b is bath energy, were determined using the algorithm described in Section 6.2 for the complete vibrational space, $\mathbf{Q^{27}}$. Overall, 174,138 $\mathbf{B}_{\mathrm{X}}^{24}$ states and 201,425 $\mathbf{B}_{\mathrm{A}}^{24}$ states were directly counted for $E_b < 0.7$ eV, compared to the 439,775 $\mathbf{Q^{27}}$ states. Due to the fewer degrees of freedom in the bath calculations, the effective number of oscillators at the $E_b = 0.7$ eV stitching point was reduced to $n^* = 9.0$ (from 9.5). For illustration, the $P_{\mathbf{B}_{\mathrm{A}}^{24}}(E_b)$ energy distribution for $\mathbf{B}_{\mathrm{A}}^{24}$ at $T = 1000$ K is shown in Figure 12. It is similar to the complete-space distribution in Figure 11d, but the maximum is shifted to slightly lower energy. The corresponding $\mathbf{B}_{\mathrm{X}}^{24}$ distribution (not shown) is very similar.

We will now model the hot Ph^- spectra by assuming that their intensity is derived from the FC-active modes only: the bath modes are "dark", and their effect is limited to increasing the degeneracy of each active-space state. This is not the same as stating that the bath *states* (as opposed to the bath *modes*) are dark. Under the dark-bath approximation, any state $\left|\{n_i''\},\{n_j''\}\right\rangle$, where $\{n_i''\} \in \mathbf{Q_X^3}$ or $\mathbf{Q_A^3}$, $\{n_j''\} \in \mathbf{B_X^{24}}$ or $\mathbf{B_A^{24}}$, is assigned the same FC spectrum as the active-space state $|\{n_i''\}\rangle$. Then, any pure-bath state $\left|\{0_i''\},\{n_j''\}\right\rangle$ has the same set of FC factors as the ground state of phenide, $|0''\rangle$. These integrals all correspond to the $\{n_i'\} \leftarrow \{0_i''\}$ active-mode excitations within $\mathbf{Q_X^3}$ or $\mathbf{Q_A^3}$, while keeping the bath part of the initial state unchanged.

The FC factors, $\mathrm{FCF}(n', n'')$, for $n', n'' \in \mathbf{Q}_{\mathrm{X}}^3$ and $\mathbf{Q}_{\mathrm{A}}^3$ were calculated in Section 5.3 (runs X5 and A2). In the dark-bath approach, the intensity of each active-space transition, $\mathrm{FCF}^2(n', n'')$, is scaled by the bath degeneracy, $g_b(E_b)dE_b$, where g_b is the bath DOS (either $g_{\mathbf{B}_{\mathrm{X}}^{24}}$ or $g_{\mathbf{B}_{\mathrm{A}}^{24}}$) computed above. The result is weighted by the Boltzmann factor for the total anion energy, $E'' =$

$E_a + E_b$, where E_a corresponds to the FC-active modes. Since each active-space transition can be coupled with any amount of thermal bath excitation, the result is integrated with respect to E_b:

$$I(n', n'') = \mathrm{FCF}^2(n', n'') \int_0^\infty g_b(E_b) e^{-(E_a + E_b)/kT} dE_b \tag{2}$$

giving the FC intensity of the $n' \leftarrow n''$ active-space transition for the initial state n'' coupled to the dark bath. The complete photoelectron spectrum is then given, as usual, by the sum of all Wigner-scaled (as defined in Section 5.1) $n' \leftarrow n''$ transition intensities, convoluted with a broadening function.

The $e^{-E_a/kT}$ part of the Boltzmann factor in Eq. 2 can be moved outside the bath integral, turning the remainder into the bath-distribution's, $P_{\mathbf{B}_\mathbf{X}^{24}}(E)$ or $P_{\mathbf{B}_\mathbf{A}^{24}}(E)$, normalization constant. For this mathematical reason, the dark-bath results are indistinguishable from the isolated active-space method described in Section 5.4, despite the inclusion of a large volume of additional information (the bath DOS). To be sure, we verified that the model spectra obtained using Eq. 2 are the same as those shown Figure 9a and 10a-c (at the same temperatures). The physical origin of this equivalence is in both models ascribing all spectral intensity to the FC-active space. In both cases, the model outcomes are determined by the active-mode temperature, whether it is maintained in isolation or in equilibrium with a bath.

The equivalence of the active-space and dark-bath models allows us to address the exaggerated compared to the experiment intensity of the origin peak in the A band simulated spectrum in Figure 9a. The spectrum shown can be calculated using either model, but we will now discuss its origin peak within the dark-bath framework. This model assigns the same FC fingerprint, $F_{|0''\rangle}(n')$ corresponding to the ground state of Ph^-, to all pure-bath states $\left|\{0_i''\}, \{n_j''\}\right\rangle$, $\{n_i''\} \in \mathbf{Q}_\mathbf{A}^\mathbf{3}$, $\{n_j''\} \in \mathbf{B}_\mathbf{A}^\mathbf{24}$. As seen in Figure 8, the corresponding FC spectrum is dominated by the band origin ('o'). In the Boltzmann-weighted average of many bath states in Eq. 2, the origin peak is amplified by the effect of the large bath degeneracy, with every bath state contributing at the same eBE as the active-space $|0'\rangle \leftarrow |0''\rangle$ transition. In the experimental spectrum, on the other hand, different bath states contribute at slightly varying eBEs, because of the differences between the anion and neutral vibrational frequencies. Our formulation of the dark-bath model does not take these state-dependent shifts into account, but we have verified that, on average, they have only a small effect on the highly averaged model spectrum overall. Neglecting these shifts,

however, leads to the exaggerated narrow peak at the transition's origin.

6.4. The bright-bath model. The $\mathbf{Q}_{\mathrm{X}}^{3}$ and $\mathbf{Q}_{\mathrm{A}}^{3}$ FC-active spaces are each spanned by the three modes most active in the photodetachment of cold phenide. The bath states (including the active-bath combination states) were excluded from the active-space model in Section 5.4. The dark-bath approximation in Section 6.3 considered their contribution to the partition function but did not assign the bath modes any FC amplitudes. We will now consider that these modes may not be necessarily dark. Although most FC activity in cold anions is due to the FC-active modes, various couplings, such as the anharmonicity and vibronic effects,[10,21,59] may light up the bath modes in the mixed states and even change the spectral shapes entirely. In the following, we will assume that all vibrations should be treated as "bright", thus rendering the active vs. bath distinction moot.

Under this approximation, the excited anion states are viewed as strongly mixed and as a result the $\mathbf{Q}_{\mathrm{X}}^{3}$ or $\mathbf{Q}_{\mathrm{A}}^{3}$ zeroth-order states share the FC amplitudes with the bath states. As a statistical postulate, we will assume that each state degenerate with a given active-space state has the same FC fingerprint as the latter. In practice, this means that the previously determined (Section 5.4) intensity of each active-space transition, $\mathrm{FCF}^2(n', n'')$, $n', n'' \in \mathbf{Q}_{\mathrm{X}}^{3}$ or $\mathbf{Q}_{\mathrm{A}}^{3}$, must be scaled by the anion density of states $g(E'')$ and weighted by the corresponding Boltzmann factor:

$$I(n', n'') = \mathrm{FCF}^2(n', n'')g(E'')e^{-E''/kT} \tag{3}$$

In contrast to Eq. 2, here E'' is not partitioned between the active space and the bath, hence no integration with respect to the latter. The total spectrum is calculated, as usual, via a Wigner-scaled sum of all $n' \leftarrow n''$ transitions, convoluted with an eKE-dependent broadening function.

Starting again with band A, Figure 13 shows the bright-bath results. The best agreement with the experiment is achieved at T = 750 K, with the 650 K and 900 K spectra included to illustrate the model's sensitivity to T. The 750 K temperature determined using the bright-bath model is several-fold lower than the active-space-only or dark-bath temperature of 3400 K (Figure 9a). This could be expected, because with more vibrational modes contributing to the transitions, the temperature needed to achieve a similar total excitation is much smaller.

Figure 14a presents the bright-bath simulation of the entire 355 nm spectrum (bands X and A), while b and c show the corresponding simulations of the X band at 532 and 611 nm. As with other approaches, we focus on the low-eBE (left) sides of the bands. Again, it is encouraging that

both bands in the 355 nm spectrum are described by the consistent bright-bath temperature of 750 K. Similar to the dark-bath case, the bright-bath temperatures of the 532 and 611 nm spectra are lower: 620 and 600 K, respectively. As in the dark-bath case, it is impossible to model both the left and right sides of band X using the same T.

It is not surprising that this model performs poorly in the high-eBE part of band X (the corresponding part of A is not accessed in the experiment). This part of the band is due to transitions from the lower anion states to higher-energy states of the neutral. The low anion states should be well-described within the uncoupled-modes approximation. Hence, the bath-coupling model likely overestimates these transitions. The statistical mixing assumption is more reasonable in the low-eBE part of the spectrum, which corresponds to highly excited anions.

6.5. Energy conservation. The common assumption of the models described so far is that the spectral signatures of various states can be predicted, on average, based on the signatures of a subset of states. Variations of this approach provide insight into the hot-band behavior and yield reasonable agreements with the experimental spectra, some limitations notwithstanding.

We will now model the hot-ion spectra without state-specific FC factors for the excited anion states. Our final approach assumes that due to the large DOS and state mixing, the state-specific spectral envelopes are subject to only one principal constraint: the conservation of energy. This approach is illustrated schematically in Figure 15. Parts a and b show the transitions from the ground and excited vibrational states of the anion. In each case, the accessed part of the neutral potential is highlighted with a color gradient. To the left are the schematic depictions of the expected bands, S_0 and $S_{E''}$, plotted as functions of the neutral energy, E'. The excited-state spectrum in b is expected to be broader than that of the $|0''\rangle$ state in a. In each case, the lowest neutral state accessed corresponds to $E' = 0$. For the ground state of the anion ($E'' = 0$), the lowest-eBE transition corresponds to the adiabatic EA, while for the excited anion, the lowest transition's eBE is reduced by the vibrational excitation of the anion (i.e., EA − E''). The two bands from a and b are plotted together with respect to the common eBE scale in Figure 15c.

Using Figure 15c as a guide, we will postulate that the spectrum of an excited anion state at energy E'', $S_{E''}$(eBE), can be obtained via a linear transformation of the $|0''\rangle$ spectrum, S_0(eBE). All $S_{E''}$(eBE) spectra discussed here are defined by the FC overlaps only, i.e., they are calculated *prior* to the Wigner, Boltzmann, and DOS scalings. For S_0(eBE), we use the cold model spectra for bands X and A obtained in Section 5.2. The S_0(eBE) → $S_{E''}$(eBE) transform assumes an

anchor point to right of the transition's VDE and is defined to shift the band's onset from eBE = EA in S_0(eBE) to eBE = EA − E'' in $S_{E''}$(eBE), as explained in the Figure 15c caption. The final photoelectron spectrum is calculated by applying the Boltzmann, Wigner, and DOS scalings to $S_{E''}$(eBE) and integrating over the full range of anion energies:

$$S(\mathrm{eBE}) = (h\nu - \mathrm{eBE})^P \int_0^\infty S_{E''}(\mathrm{eBE}) g(E'') e^{-E''/kT} dE'' \quad (4)$$

The results are shown in Figure 16. The low-eBE scaling of the model bands is affected the most by temperature, while the anchor parameter in the S_0(eBE) → $S_{E''}$(eBE) transformation controls the position of the maximum and is therefore easy to choose. (For the model spectra in Figure 16, the X band anchor was set at eBE = 1.75 eV, while that for A at eBE = 3.80 eV.) The agreement of the model spectra with the experiment is much improved compared to the other models, particularly for the X band. The model assigns a consistent temperature of 700 K to the experimental X bands observed at each wavelength. The A band, however, is described by T = 500 K (Figure 16a), but this apparent discrepancy has a straightforward explanation.

Due to the σ and π characters of the respective detachment orbitals (Figure 4), transition X involves a more significant Ph^- to Ph geometry change compared to A. Therefore, the X band has a broader FC spectrum due to a broad range of neutral vibrational states accessed from any of the anion states. The energy-conservation model assumes that the low-eBE onset of band X corresponds to transitions from the highest anion levels with detectable populations to the $|0'\rangle$ state of σ-Ph. This assumption is valid only for a broad-band transition like X.

Due to the smaller geometry change, band A is narrow in comparison. The most intense transition from the $|0''\rangle$ state of Ph^- is to the $|0'\rangle$ state of π-Ph (see the FC stick spectrum in Figure 8). The most intense transitions from excited Ph^- levels are expected to be to the corresponding excited π-Ph states. For large enough E'', the $|0'\rangle$ state will not be accessed at all—not because of the energetics but due to the Franck-Condon considerations, which this model disregards. This would mean that the low-eBE onset of band A does not correspond to transitions to the $|0'\rangle$ state of π-Ph. In this case, the energy-conservation model overestimates the band width for a given temperature and, vice versa, underestimates the temperature for a given band width. This is what we see in Figure 16a and hence, the X band temperature of 700 K, rather than A band's 500 K, should be viewed as a more reliable estimate of the true anion temperature.

7. Summary and Conclusions

We reported the photoelectron spectra of hot phenide obtained at 355 nm (3.49 eV), 532 nm (2.33 eV), and 611 nm (2.03 eV). Because of the very large number of initial vibrational states involved, these broad and congested spectra cannot be analyzed using complete Franck-Condon calculations, while the active-modes analysis is strictly applicable to cold anions only. Hence, we have described several model approaches that combine the results of a limited (and, therefore, feasible) Franck-Condon analysis with statistical calculations to interpret the observed spectra. We stress that limiting the FC calculations for hot ions to a subset of vibrational modes stems from the computational necessity, not physical reality, for all modes should be viewed as active with respect to thermal excitation.

Comparison of the model results to the experimental spectra provides insight into the electronic/vibrational structure and the statistical nature of hot polyatomic ions. The statistical approach also provides efficient means of determining the ion temperature by modeling the experimental spectra. This capability can be applied to the properties of hot plasmas, the collisional excitation or cooling of ions, as well as the evaporative cooling in cluster ions.

Table 4 provides a summary of the temperatures determined using the models described in this work. The isolated active modes and active modes + dark bath models ascribe the photoelectron spectra to excitations within the FC-active modes only. The former model does not consider the FC-inactive vibrations at all, while the latter accounts only for the degeneracy due to the inactive modes. These two models yield identical results, because the predicted spectra depend on the active-mode temperature only, whether these modes are isolated or in thermodynamic equilibrium with the other, dark modes. As a consequence of confining all spectral hot bands to a small subset of vibrational modes, the ion temperatures obtained by comparing these models to the experimental spectra are presumed to be much higher than the real temperature of the ions.

The other two models in Table 4 consider couplings of the FC-active modes to the bath, including sharing of the transition intensities. As the “dark” modes light up, the active/bath distinction disappears, but it is maintained within the model formalism in the form of the explicit assumption that the FC signatures of the active space can be extrapolated to the rest of the coupled vibrations. This extrapolation can be done in one of two ways. The active modes + bright bath model assigns the bath states the same FC factors as those of the degenerate active-space states. This approach yields more realistic ion temperatures but overestimates the contribu-

tions of the higher-eBE transitions from the low-energy anion states to the excited states of the neutral. The second coupling approach is based on the energy conservation only and does not consider the FC factors for the excited anion states explicitly. Instead, it uses a linear transformation of the ground-state spectrum to predict the excited-state spectra. This model yields a consistent ion temperature of 700 K, determined based on the X band at all laser wavelengths used. The A model temperature proved to be lower, but due to the reasons discussed in Section 6.5 this discrepancy does not affect our ion temperature estimate. It is our overarching assertion that 700 K is the approximate vibrational temperature of the ions in the reported experiments.

In conclusion, we recognize the unique features of high temperature polyatomic ions stemming from their rapidly increasing with energy density of states. The described formalism provides an efficient way for combining limited state-specific quantum calculations with statistical analysis to predict the envelopes of the congested photoelectron spectra of hot ions.

AUTHOR INFORMATION

Corresponding Author

*Email: sanov@arizona.edu

ORCID

Beverly Ru: 0000-0003-1258-6224
Andrei Sanov: 0000-0002-2373-4387

Author Contributions

The manuscript was written through contributions of all authors. All authors have given approval to the final version of the manuscript.

Funding Sources

U.S. National Science Foundation Grant CHE-2153986.

Notes

The authors declare no competing financial interest.

ACKNOWLEDGMENTS

We thank Professor Samer Gozem for advice on FC calculations using the ezFCF program[43] and Professor Steven D. Schwartz for comments on the manuscript. This research is supported by the U.S. National Science Foundation through grant CHE-2153986.

References

1. McQuarrie, D. A., *Statistical Mechanics*. University Science Books: Sausalito, California, 2000.
2. Gilbert, R. G.; Smith, S. C., *Theory of unimolecular and recombination reactions*. Blackwell Scientific Publications: Oxford, England, 1990.
3. Hill, T. L., *An Introduction to Statistical Thermodynamics*. Dover Publications: New York, 2012.
4. Grebowsky, J. M.; McKelvey, J. P., Density-of-States Function for the Harmonic Oscillator: A Simple and Direct Approach. *Am. J. Phys.* **1967,** *35*, 352-353.
5. Franck, J.; Dymond, E. G., Elementary processes of photochemical reactions. *Trans. Faraday Soc.* **1926,** *21*, 536-542.
6. Condon, E., A Theory of Intensity Distribution in Band Systems. *Phys. Rev.* **1926,** *28*, 1182-1201.
7. Condon, E. U., The Franck-Condon Principle and Related Topics. *Am. J. Phys.* **1947,** *15*, 365-374.
8. Dierksen, M.; Grimme, S., An efficient approach for the calculation of Franck–Condon integrals of large molecules. *J. Chem. Phys.* **2005,** *122*, 244101.
9. Santoro, F.; Improta, R.; Lami, A.; Bloino, J.; Barone, V., Effective method to compute Franck-Condon integrals for optical spectra of large molecules in solution. *J. Chem. Phys.* **2007,** *126*, 084509.
10. Jankowiak, H.-C.; Stuber, J. L.; Berger, R., Vibronic transitions in large molecular systems: Rigorous prescreening conditions for Franck-Condon factors. *J. Chem. Phys.* **2007,** *127*, 234101.
11. Borrelli, R.; Capobianco, A.; Peluso, A., Franck–Condon factors—Computational approaches and recent developments. *Can. J. Chem.* **2013,** *91*, 495-504.
12. Firth, R. A.; Dimino, T. L.; Gichuhi, W. K., Negative Ion Photoelectron Spectra of Deprotonated Benzonitrile Isomers via Computation of Franck–Condon Factors. *J. Phys. Chem. A* **2022,** *126*, 4781-4790.
13. Johnson, M. A.; Lineberger, W. C., Pulsed Methods for Cluster Ion Spectroscopy. In *Techniques for the Study of Ion Molecule Reactions*, Farrar, J. M.; Saunders, W. H., Eds. Wiley: New York, 1988; pp 591-635.
14. Nadal, M. E.; Kleiber, P. D.; Lineberger, W. C., Photofragmentation of Mass-Selected $ICl^-(CO_2)_n$ Cluster Ions: Solvation Effects on the Structure and Dynamics of the Ionic Chromophore. *J. Chem. Phys.* **1996,** *105*, 504-514.
15. Surber, E.; Ananthavel, S. P.; Sanov, A., Nonexistent electron affinity of OCS and the stabilization of carbonyl sulfide anions by gas phase hydration. *J. Chem. Phys.* **2002,** *116*, 1920-1929.
16. Creighton, J. A.; Lippincott, E. R., Vibrational Frequency and Dissociation Energy of the Superoxide Ion. *J. Chem. Phys.* **1964,** *40*, 1779-1780.
17. Holzer, W.; Murphy, W. F.; Bernstein, H. J.; Rolfe, J., Raman spectrum of O2− ion in alkali halide crystals. *J. Mol. Spectrosc.* **1968,** *26*, 543-545.
18. Ervin, K. M.; Ho, J.; Lineberger, W. C., Ultraviolet Photoelectron Spectrum of NO_2^-. *J. Phys. Chem.* **1988,** *92*, 5405-5412.
19. Forney, D.; Thompson, W. E.; Jacox, M. E., The vibrational spectra of molecular ions isolated in solid neon. XI. NO[sup +][sub 2], NO[sup -][sub 2], and NO[sup -][sub 3]. *J.*

Chem. Phys. **1993,** *99*, 7393-7403.
20. Gunion, R. F.; Gilles, M. K.; Polak, M. L.; Lineberger, W. C., Ultraviolet Photoelectron-Spectroscopy of the Phenide, Benzyl and Phenoxide Anions, with ab initio Calculations. *Int. J. Mass Spectrom.* **1992,** *117*, 601-620.
21. Sivaranjana Reddy, V.; Venkatesan, T. S.; Mahapatra, S., Vibronic interactions in the photodetachment spectroscopy of phenide anion. *J. Chem. Phys.* **2007,** *126*, 074306.
22. Millar, T. J.; Walsh, C.; Field, T. A., Negative Ions in Space. *Chem. Rev.* **2017,** *117*, 1765-1795.
23. Wakelam, V.; Herbst, E., Polycyclic Aromatic Hydrocarbons in Dense Cloud Chemistry. *Astrophys. J.* **2008,** *680*, 371-383.
24. Kaiser, R. I.; Hansen, N., An Aromatic Universe–A Physical Chemistry Perspective. *J. Phys. Chem. A* **2021,** *125*, 3826-3840.
25. Jones, B. M.; Zhang, F.; Kaiser, R. I.; Jamal, A.; Mebel, A. M.; Cordiner, M. A.; Charnley, S. B., Formation of benzene in the interstellar medium. *Proc. Nat. Acad. Sci.* **2011,** *108*, 452-457.
26. Kaiser, R. I.; Parker, D. S. N.; Mebel, A. M., Reaction Dynamics in Astrochemistry: Low-Temperature Pathways to Polycyclic Aromatic Hydrocarbons in the Interstellar Medium. *Annu. Rev. Phys. Chem.* **2015,** *66*, 43-67.
27. Parker, D. S. N.; Zhang, F.; Kim, Y. S.; Kaiser, R. I.; Landera, A.; Kislov, V. V.; Mebel, A. M.; Tielens, A. G. G. M., Low temperature formation of naphthalene and its role in the synthesis of PAHs (Polycyclic Aromatic Hydrocarbons) in the interstellar medium. *Proc. Nat. Acad. Sci.* **2012,** *109*, 53-58.
28. Herbst, E., Chemistry in the Interstellar Medium. *Annu. Rev. Phys. Chem.* **1995,** *46*, 27-54.
29. Mansurov, Z. A., Soot Formation in Combustion Processes (Review). *Combust., Explos. Shock Waves (Engl. Transl.)* **2005,** *41*, 727.
30. Parker, D. S. N.; Kaiser, R. I.; Troy, T. P.; Kostko, O.; Ahmed, M.; Mebel, A. M., Toward the Oxidation of the Phenyl Radical and Prevention of PAH Formation in Combustion Systems. *J. Phys. Chem. A* **2015,** *119*, 7145-7154.
31. Surber, E.; Sanov, A., Photoelectron imaging spectroscopy of molecular and cluster anions: CS_2^- and $OCS^-(H_2O)_{1,2}$. *J. Chem. Phys.* **2002,** *116*, 5921-5924.
32. Mabbs, R.; Surber, E.; Sanov, A., Photoelectron Imaging of Negative Ions: Atomic Anions to Molecular Clusters. *Analyst* **2003,** *128*, 765-772.
33. Blackstone, C. C. Exploring the Chemistry of Methoxide with Oxygen Through Photoelectron Imaging Spectroscopy. Ph.D. dissertation, University of Arizona, Tucson, 2020.
34. Wiley, W. C.; McLaren, I. H., Time-of-Flight Mass Spectrometer with Improved Resolution. *Rev. Sci. Instrum.* **1955,** *26*, 1150.
35. Eppink, A. T. J. B.; Parker, D. H., Velocity map imaging of ions and electrons using electrostatic lenses: Application in photoelectron and photofragment ion imaging of molecular oxygen. *Rev. Sci. Instrum.* **1997,** *68*, 3477-3484.
36. Chandler, D. W.; Houston, P. L., Two-Dimensional Imaging of State-Selected Photodissociation Products Detected by Multiphoton Ionization. *J. Chem. Phys.* **1987,** *87*, 1445-1447.
37. Heck, A. J. R.; Chandler, D. W., Imaging Techniques For the Study of Chemical Reaction Dynamics. *Annu. Rev. Phys. Chem.* **1995,** *46*, 335-372.
38. Dribinski, V.; Ossadtchi, A.; Mandelshtam, V. A.; Reisler, H., Reconstruction of abel-

transformable images: The Gaussian basis-set expansion abel transform method. *Rev. Sci. Instrum.* **2002,** *73*, 2634-2642.
39. Surber, E.; Mabbs, R.; Sanov, A., Probing the electronic structure of small molecular anions by photoelectron imaging. *J. Phys. Chem. A* **2003,** *107*, 8215-8224.
40. Sanov, A.; Mabbs, R., Photoelectron imaging of negative ions. *Int. Rev. Phys. Chem.* **2008,** *27*, 53-85.
41. Shao, Y. H.; Gan, Z. T.; Epifanovsky, E.; Gilbert, A. T. B.; Wormit, M.; Kussmann, J.; Lange, A. W.; Behn, A.; Deng, J.; Feng, X. T., et al., Advances in molecular quantum chemistry contained in the Q-Chem 4 program package. *Mol. Phys.* **2015,** *113*, 184-215.
42. Krylov, A. I., Equation-of-motion coupled-cluster methods for open-shell and electronically excited species: The Hitchhiker's guide to Fock space. *Annu. Rev. Phys. Chem.* **2008,** *59*, 433-462.
43. Gozem, S.; Krylov, A. I., The ezSpectra suite: An easy-to-use toolkit for spectroscopy modeling. *Wiley Interdiscip. Rev.: Comput. Mol. Sci.* **2021,** *12*, e1546.
44. Duschinsky, F., The importance of the electron spectrum in multi atomic molecules. concerning the Franck-Condon principle. *Acta Physicochim. URSS* **1937,** *7*, 551-566.
45. Wigner, E. P., On the behavior of cross sections near thresholds. *Phys. Rev.* **1948,** *73*, 1002-1009.
46. Engelking, P. C., Strong electron-dipole coupling in photodetachment of molecular negative ions: Anomalous rotational thresholds. *Phys. Rev. A* **1982,** *26*, 740-745.
47. Lakhmanskaya, O.; Simpson, M.; Murauer, S.; Kokoouline, V.; Wester, R., Photodetachment spectroscopy of cold trapped NH_2^- near threshold. *J. Chem. Phys.* **2018,** *149*, 104302.
48. Simpson, M.; Nötzold, M.; Schmidt-May, A.; Michaelsen, T.; Bastian, B.; Meyer, J.; Wild, R.; Gianturco, F. A.; Milovanović, M.; Kokoouline, V., et al., Threshold photodetachment spectroscopy of the astrochemical anion CN^-. *J. Chem. Phys.* **2020,** *153*, 184309.
49. Dauletyarov, Y.; Ru, B.; Sanov, A., Anion of Oxalyl Chloride: Structure and Spectroscopy. *J. Phys. Chem. A* **2021,** *125*, 9865-9876.
50. Climen, B.; Pagliarulo, F.; Ollagnier, A.; Baguenard, B.; Concina, B.; Lebeault, M. A.; Lépine, F.; Bordas, C., Threshold laws in delayed emission: an experimental approach. *Eur. Phys. J. D* **2007,** *43*, 85-89.
51. Porter, G.; Ward, B., The electronic spectra of phenyl radicals. *Proc. R. Soc. London, Ser. A* **1965,** *287*, 457-470.
52. Tonokura, K.; Norikane, Y.; Koshi, M.; Nakano, Y.; Nakamichi, S.; Goto, M.; Hashimoto, S.; Kawasaki, M.; Sulbaek Andersen, M. P.; Hurley, M. D., et al., Cavity Ring-down Study of the Visible Absorption Spectrum of the Phenyl Radical and Kinetics of Its Reactions with Cl, Br, Cl_2, and O_2. *J. Phys. Chem. A* **2002,** *106*, 5908-5917.
53. Baguenard, B.; Pinaré, J. C.; Bordas, C.; Broyer, M., Photoelectron imaging spectroscopy of small tungsten clusters: Direct observation of thermionic emission. *Phys. Rev. A* **2001,** *63*, 023204.
54. Baguenard, B.; Pinaré, J. C.; Lépine, F.; Bordas, C.; Broyer, M., Thermionic emission in small carbon cluster anions. *Chem. Phys. Lett.* **2002,** *352*, 147-153.
55. Surber, E.; Sanov, A., Imaging of Direct Photodetachment and Autodetachment of $(OCS)_2^-$: Excited-State Dynamics of the Covalent Dimer Anion. *Phys. Rev. Lett.* **2003,** *90*, 093001.
56. Surber, E.; Sanov, A., Photoelectron imaging of carbonyl sulfide cluster anions: Isomer coexistence and competition of excited-state decay mechanisms. *J. Chem. Phys.* **2003,** *118*,

9192-9200.
57. Adams, C. L.; Hansen, K.; Weber, J. M., Vibrational Autodetachment from Anionic Nitroalkane Chains: From Molecular Signatures to Thermionic Emission. *J. Phys. Chem. A* **2019,** *123*, 8562-8570.
58. Stockett, M. H.; Bull, J. N.; Schmidt, H. T.; Zettergren, H., Statistical vibrational autodetachment and radiative cooling rates of para-benzoquinone. *Phys. Chem. Chem. Phys.* **2022,** *24*, 12002-12010.
59. Sharma, K.; Miller, T. A.; Stanton, J. F., Vibronically coupled states: computational considerations and characterisation of vibronic and rovibronic spectroscopic parameters. *Int. Rev. Phys. Chem.* **2021,** *40*, 165-298.

Table 1. Geometric parameters describing the equilibrium structures of Ph^-, σ-Ph, and π-Ph. Each structure is planar, of C_{2v} symmetry. The carbon atom numbers (1-6) are defined in Figure 5. Bondlengths are in Angstroms, angles in degrees.

	Ph^- (X^1A_1)[a]		σ-Ph (X^2A_1)[b]	π-Ph (A^2B_1)[c]
C1–C2	1.423	1.436	1.380	1.480
C2–C3	1.407	1.415	1.407	1.387
C3–C4	1.402	1.410	1.400	1.426
C2–H	1.102	1.104	1.091	1.097
C3–H	1.099	1.102	1.092	1.096
C4–H	1.094	1.098	1.090	1.095
C2–C1–C6	112.1	111.2	125.9	111.7
C1–C2–C3	124.9	125.3	116.5	124.7
C3–C4–C5	118.2	118.0	120.6	120.5
H–C2–C3	116.1	116.0	121.0	118.2
H–C3–C2	120.4	120.4	119.6	121.5

[a] First value: B3LYP/aug-cc-pVDZ. Second: CCSD/aug-cc-pVDZ

[b] B3LYP/aug-cc-pVDZ

[c] EOM-IP-CCSD/aug-cc-pVDZ

Table 2. Harmonic frequencies (in cm^{-1}) and symmetry species of the vibrational normal modes of Ph^-, σ-Ph, and π-Ph.[a]

Mode number	$Ph^-(X\,^1A_1)$		σ-Ph ($X\,^2A_1$)		π-Ph ($A\,^2B_1$)	
1	351	A_2	398	A_2	287	A_2
2	399	B_1	422	B_1	354	B_1
3	**591**	**A_1**	596	B_2	519	B_2
4	627	B_2	**616**	**A_1**	**579**	**A_1**
5	668	B_1	669	B_1	690	B_1
6	723	B_1	710	B_1	794	A_2
7	842	A_2	803	A_2	817	B_1
8	858	B_1	881	B_1	922	B_1
9	951	A_2	955	A_2	**924**	**A_1**
10	**958**	**A_1**	**980**	**A_1**	976	A_2
11	961	B_1	983	B_1	**991**	**A_1**
12	**1000**	**A_1**	**1017**	**A_1**	996	B_1
13	1041	B_2	1046	A_1	1016	A_1
14	1049	A_1	1069	B_2	1054	B_2
15	1143	B_2	1167	A_1	1103	B_2
16	1181	A_1	1167	B_2	1209	A_1
17	1270	B_2	1292	B_2	1254	B_2
18	1322	B_2	1334	B_2	1327	B_2
19	1412	B_2	1449	B_2	1383	B_2
20	1436	A_1	1458	A_1	1439	A_1
21	**1560**	**A_1**	**1572**	**A_1**	1533	B_2
22	1568	B_2	1630	B_2	**1626**	**A_1**
23	3017	A_1	3166	A_1	3173	A_1
24	3019	B_2	3171	B_2	3175	B_2
25	3065	A_1	3184	A_1	3193	A_1
26	3070	B_2	3186	B_2	3200	B_2
27	3134	A_1	3197	A_1	3215	A_1

[a] The Ph^- and σ-Ph frequencies were calculated using the B3LYP/aug-cc-pVDZ method. EOM-IP-CCSD/aug-cc-pVDZ was used for π-Ph. The symmetry labels within the C_{2v} point group are defined using the standard Mulliken notation. The bolded/shaded cells correspond to the normal modes included in Figure 5.

Table 3. Benchmarking details of the FC factor calculations using ezFCF.

Run	Modes included	Max excitations Anion	Max excitations Neutral	Vibrational states Anion	Vibrational states Neutral	No. of comb. bands	Apprx. time[a]
X1	27 (all)	24	24	6.26×10^{9}	6.26×10^{9}	3.92×10^{19}	8×10^{6} yrs
X2	27 (all)	10	10	3.48×10^{8}	3.48×10^{8}	1.21×10^{17}	25,000 yrs
X3	27 (all)	0	10	1	3.48×10^{8}	3.48×10^{8}	40 min
X4	10 (all A_1)	0	16	1	5.31×10^{6}	5.31×10^{6}	<1 min
X5	3 ($\mathbf{Q}_X^3$)	24	24	2925	2925	8.56×10^{6}	<1 min
X6	2 (ν'_4, ν'_{10})	24	24	325	325	1.06×10^{5}	1 sec
A1	27 (all)	0	4	1	31465	31465	<1 sec
A2	3 ($\mathbf{Q}_A^3$)	24	24	2925	2925	8.56×10^{6}	<1 min
A3	3 ($\mathbf{Q}_A^3$)	8	8	165	165	27225	<1 sec

[a] The calculations were carried out on an Intel Core i7-7700HQ 2.80 GHz processor using 16 GB of RAM.

Table 4. Model temperatures.

Model	Section	Figures	X band[a]	A band
FC active modes only	5.4	9a, 10	3400 K 3000 K 3000 K	3400 K
FC active modes + dark bath	6.3	9a, 10	3400 K 3000 K 3000 K	3400 K
FC active modes + bright bath	6.4	13, 14	750 K 620 K 600 K	750 K
Energy conservation	6.5	16	700 K 700 K 700 K	500 K

[a] The three values listed for each model correspond to the 355, 532, and 611 nm spectra, respectively.

Figure 1

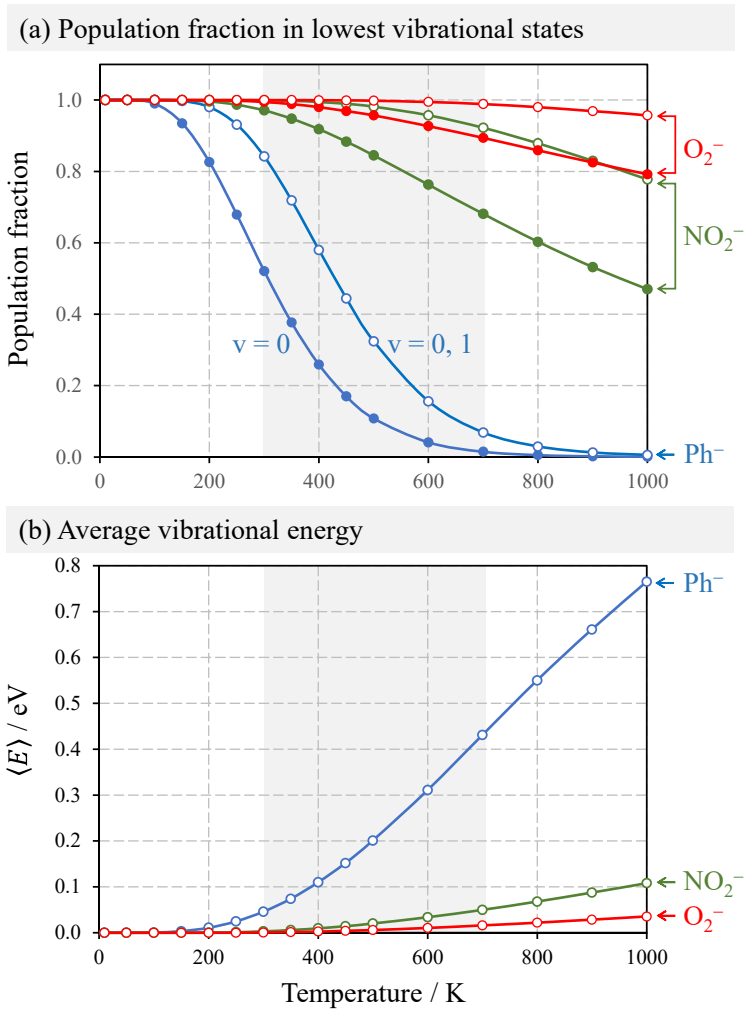

Figure 1. Temperature-dependent statistical properties of Ph^- (blue), NO_2^- (green), and O_2^- (red) for T = 0-1000 K. Shaded areas highlight the 300-700 K range. (a) Closed circles: fractional population of the ground vibrational state (labeled as v = 0). Open circles: the combined fractional populations of the ground state and all singly excited states (labeled as v = 0, 1). (b) Average vibrational energies of the ions.

Figure 2

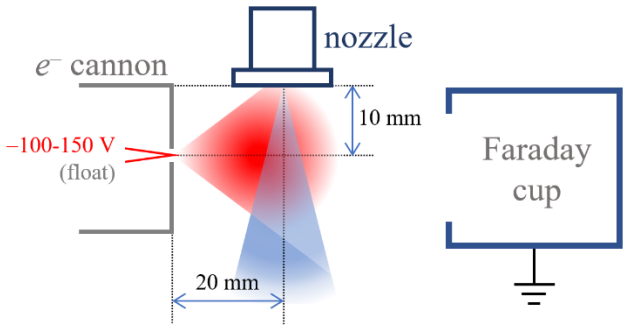

Figure 2. Schematic depiction of the electron-impact ionization ion source with an electron cannon.

Figure 3

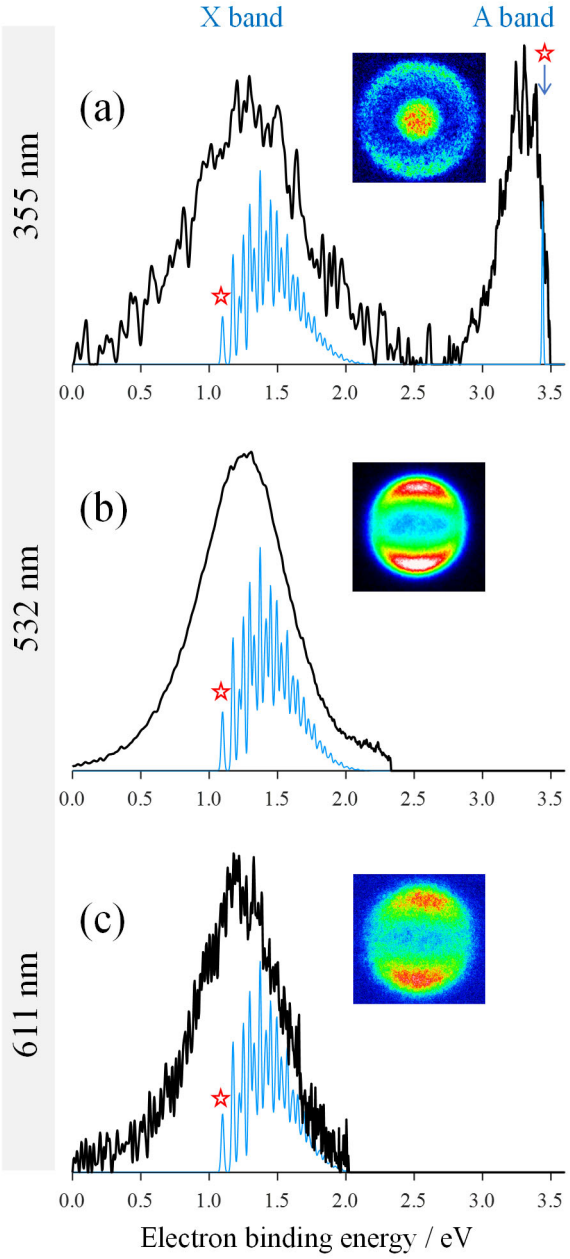

Figure 3. Photoelectron images and spectra (black) of Ph^- obtained at (a) 355 nm, (b) 532 nm, and (c) 611 nm. The laser polarization direction is vertical in the plane of all images. Light blue: the model spectra of cold phenide, obtained as described in Section 5.2 (ezFCF run X3 in Table 3), included here for comparison. The model peaks marked with stars are the corresponding transition origins.

Figure 4

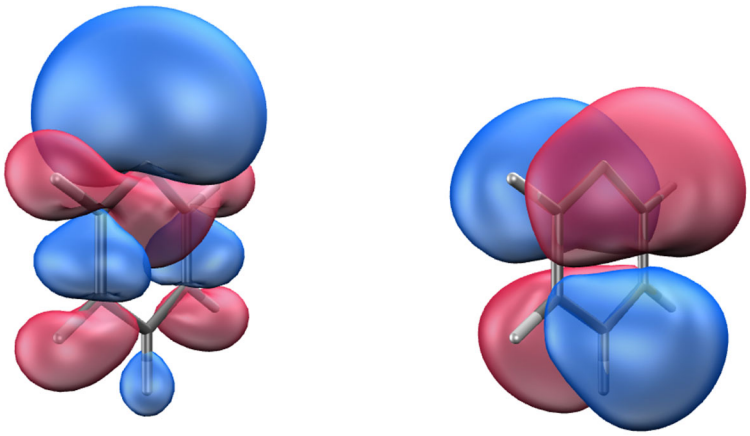

HOMO HOMO−1

Figure 4. Canonical Hartree-Fock molecular orbitals of the phenide anion: σ (a_1) HOMO and π (b_1) HOMO−1. Calculated at the optimized anion geometry with the aug-cc-pVDZ basis set. Isosurface value = 0.04.

Figure 5

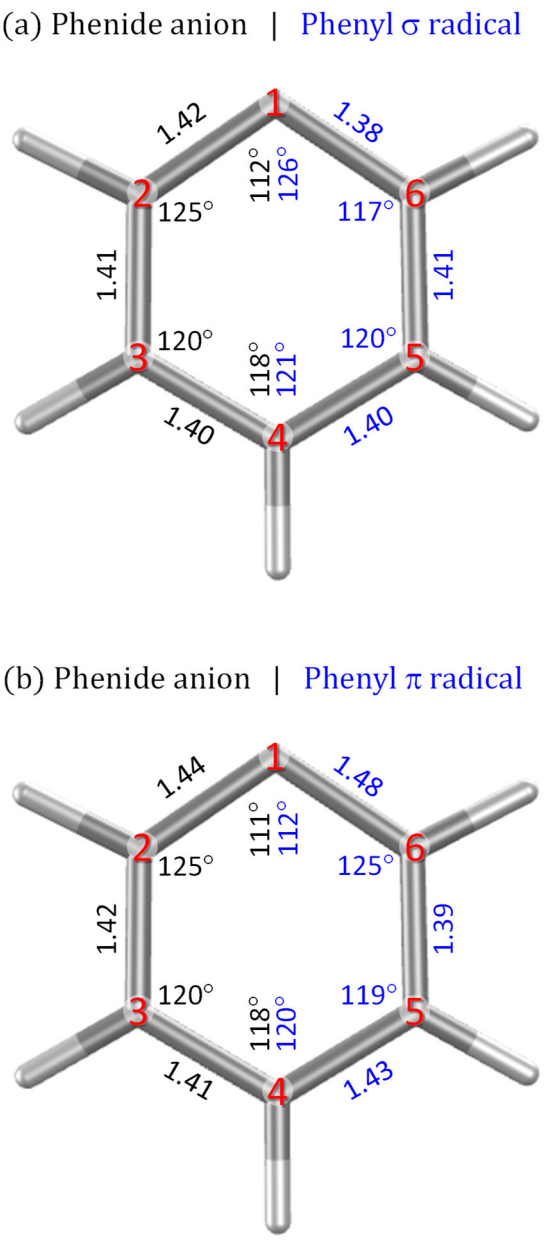

Figure 5. The equilibrium geometries of (a) Ph^- vs. σ-Ph and (b) Ph^- vs. π-Ph. In each part, a single molecular frame is shown for the anion and the neutral. The geometric parameter values on the left are for the anion, on the right—the neutral. The complete parameters are given in Table 1. Both the anion and neutral structures in (a) were optimized at the B3LYP level. In (b), CCSD was used for the anion and EOM-IP-CCSD for π-Ph.

Figure 6

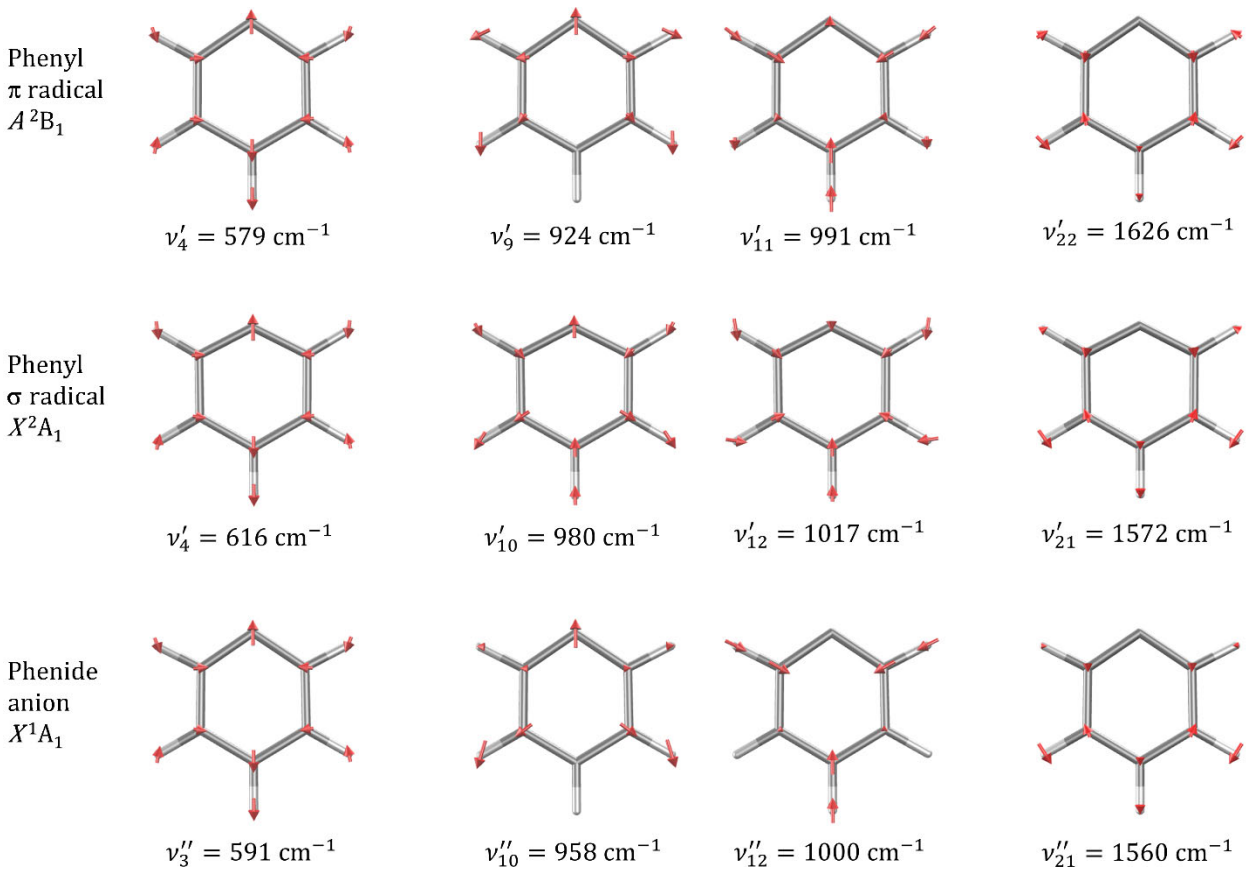

Figure 6. The coordinates and fundamental frequencies of several A_1-symmetry normal vibrational modes of Ph^- (bottom), σ-Ph (middle), and π-Ph (top), included in the FC-active spaces, as discussed in Section 5.3. The same modes are highlighted and bolded in Table 2.

Figure 7

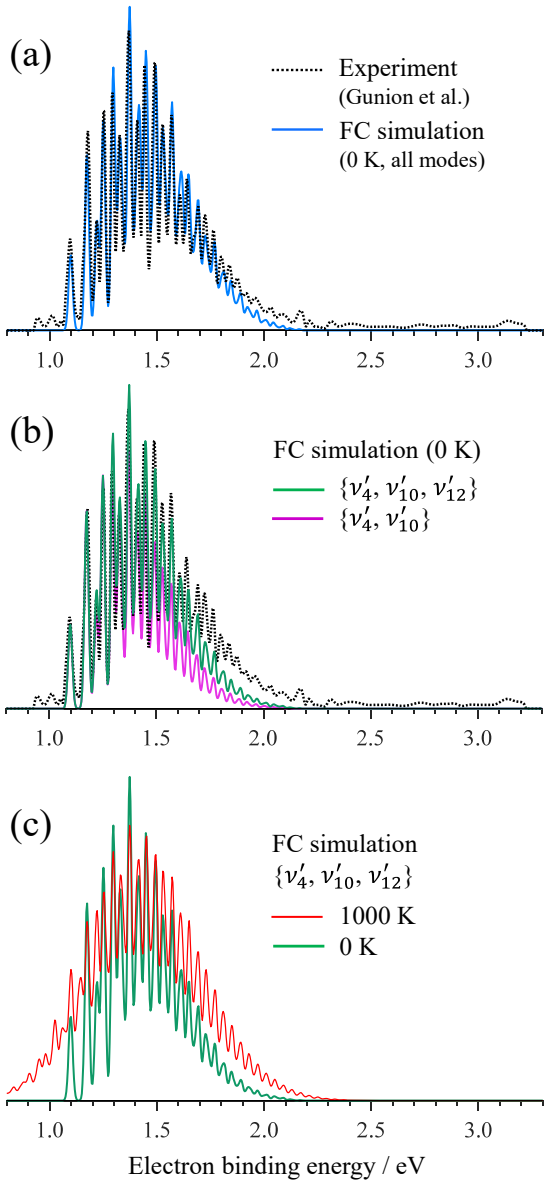

Figure 7. FC simulations of the σ-Ph ← Ph^- transition (band X) in phenide obtained under various conditions. (a) The blue trace includes is based on ezFCF run X3 (Table 3), which included all 27 vibrational modes of σ-Ph, with no excitations permitted in the anion ($T = 0$). (b) Purple: ν_4' and ν_{10}' modes of σ-Ph only (run X6); green: the ν_4', ν_{10}', and ν_{12}' modes only, corresponding to the $\mathbf{Q}_X^3$ vibrational space (run X5); both spectra are similarly normalized and correspond to $T = 0$. The black dotted trace in both (a) and (b) is the 351 nm experimental spectrum obtained by Lineberger and co-workers at approximately 300 K (Ref. [20]). (c) Green: the same $\mathbf{Q}_X^3$, $T = 0$ spectrum as in (b). Red: similar $\mathbf{Q}_X^3$ spectrum based on run X5 with $T = 1000$ K. Additional modeling details are provided in the text.

Figure 8

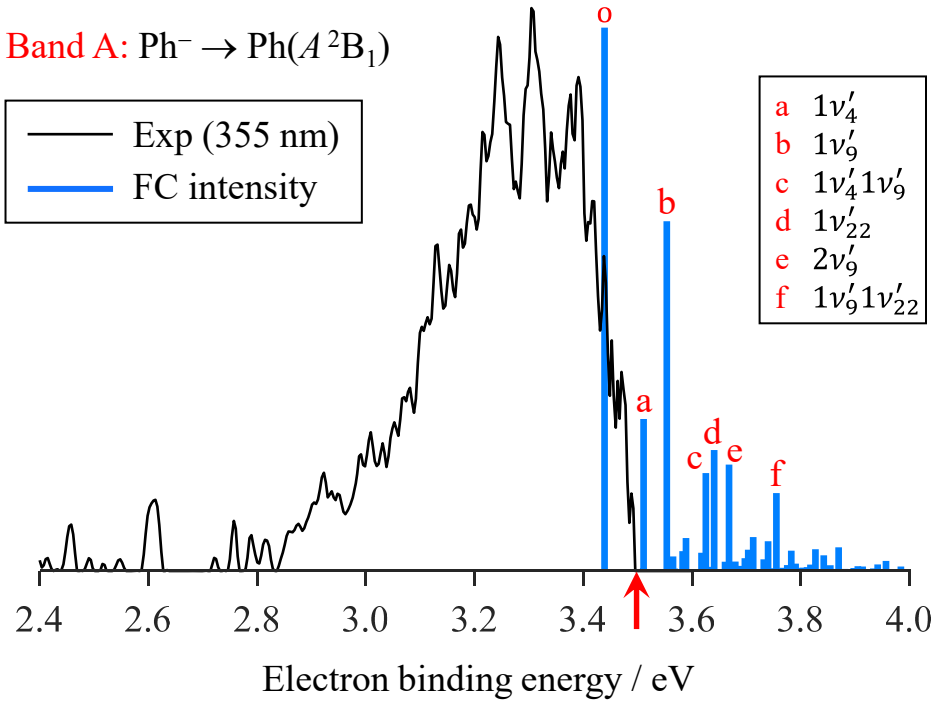

Figure 8. Blue: the FC stick spectrum of the A band (run A1, $T = 0$, uncorrected for the photon energy). Peak labeled 'o' is the transition origin (the 0-0 transition). Its position is based on a combination of previous experimental data from refs. 20,51-52, as described in Section 5.2. Inset shows the assignments of other most intense transitions (corresponding to the vibrational states excited in π-Ph). Additional modeling details are provided in the text. Black: the experimental A band expanded from Figure 3a. The red arrow at 3.49 eV indicates the 355 nm photon energy.

Figure 9

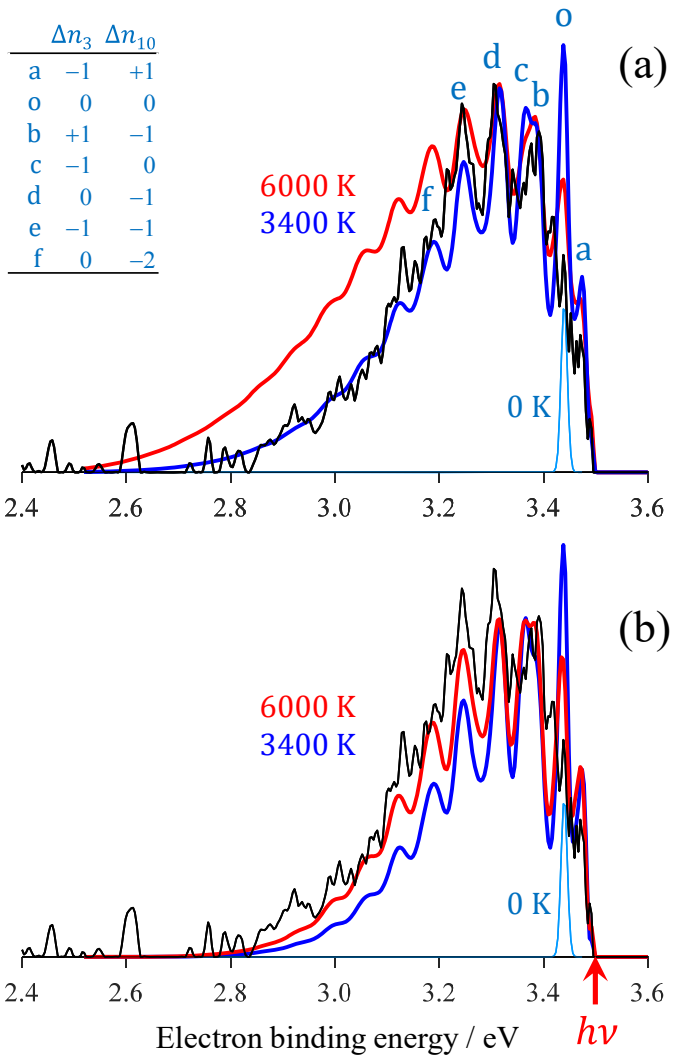

Figure 9. The (equivalent) isolated FC-active space and dark-bath models applied to band A. (a) Model spectra obtained for the $\mathbf{Q}_{\mathrm{A}}^{3}$ vibrational space, either isolated from all other modes or coupled to a "dark" $\mathbf{B}_{\mathrm{A}}^{24}$ bath as described in the text. The light blue, dark blue, and red spectra correspond to $\mathbf{Q}_{\mathrm{A}}^{3}$ temperatures of 0, 3400, and 6000 K, respectively. They were calculated by allowing up to 24 combined vibrational excitations in both the anion and neutral states (run A2). The inset gives aggregate assignments of the labeled peaks by indicating the changes in the excitation numbers n_3 and n_{10}, corresponding to the anion ν_3'' and ν_{10}'' modes, upon photodetachment. Because ν_3'' maps onto the π-Ph mode ν_4' (Figure 5), while ν_{10}'' maps onto ν_9', the changes are calculated as $\Delta n_3 = n_4' - n_3''$ and $\Delta n_{10} = n_9' - n_{10}''$. (b) Same as (a), but with no more than 8 (instead of 24) excitation quanta among the three active modes (run A3). Additional modeling details are provided in the text. The black traces in both (a) and (b) correspond to the experimental spectrum reproduced (expanded) from Figure 3a.

Figure 10

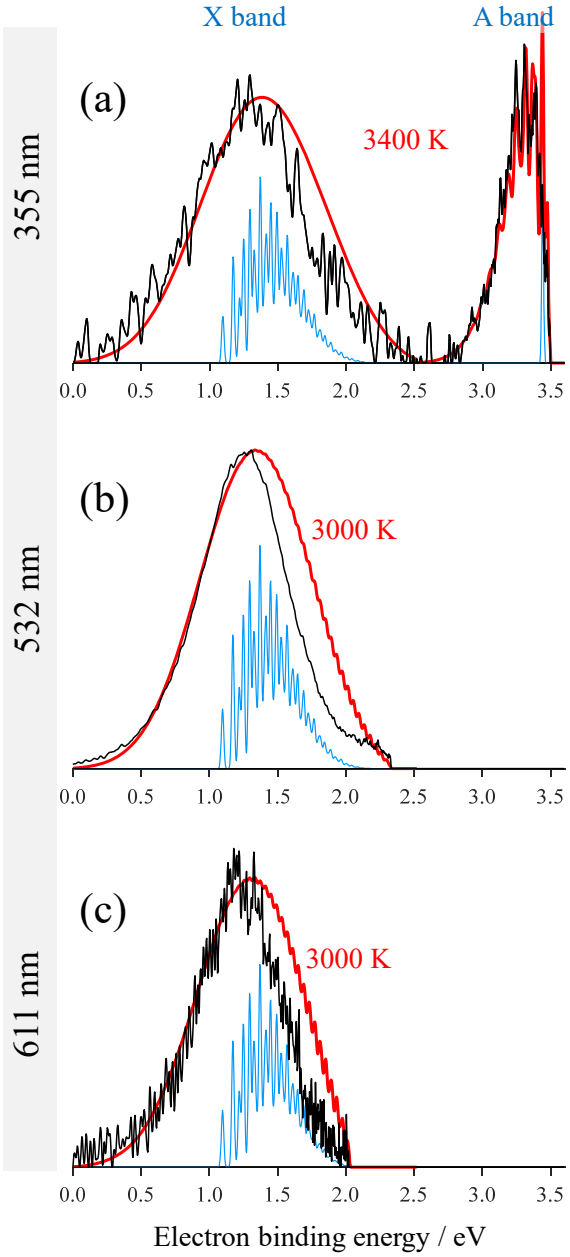

Figure 10. The (equivalent) isolated FC-active space and dark-bath models applied to bands X and A at (a) 355 nm, (b) 532 nm, and (c) 611 nm. Red: model spectra calculated at the indicated temperatures within the $\mathbf{Q}_{\mathrm{X}}^{3}$ and $\mathbf{Q}_{\mathrm{A}}^{3}$ spaces (runs X5 and A2, respectively), either isolated from all other modes, or coupled to the corresponding "dark" baths. Additional modeling details are provided in the text. Light blue: $T = 0$ all-modes FC reference spectra calculated as described in Section 5.2 (runs X3 and A1). Black: the corresponding experimental spectra reproduced for comparison from Figure 3a-c.

Figure 11

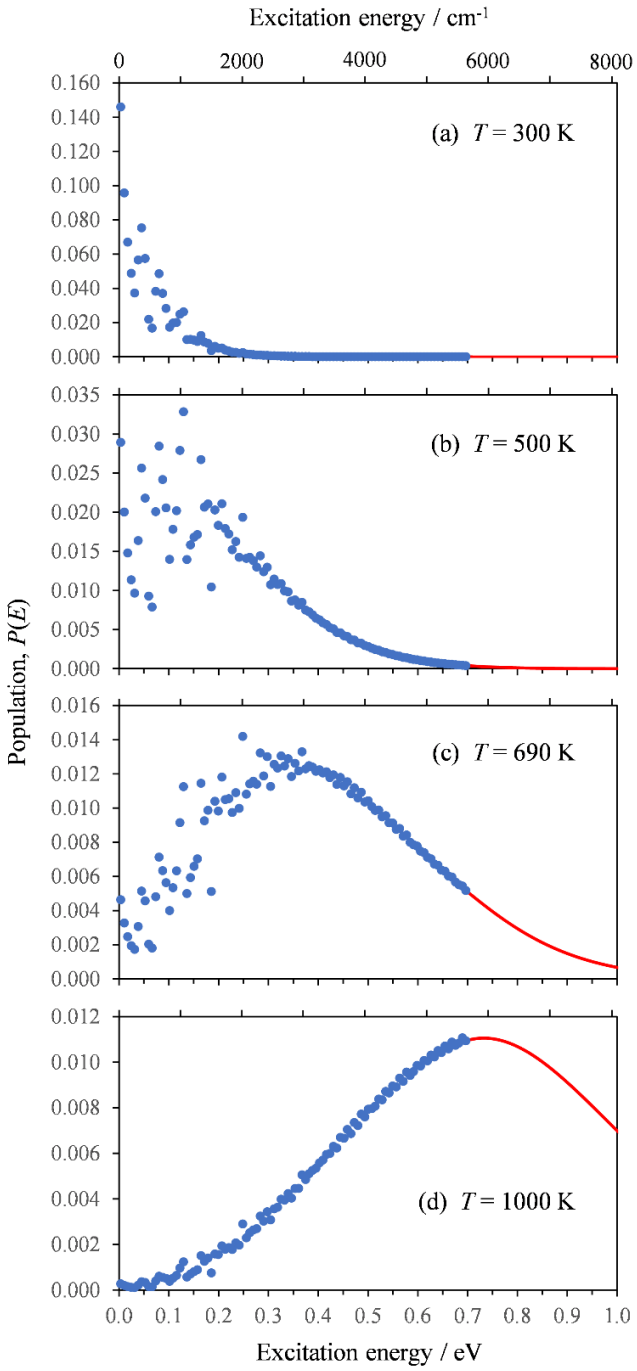

Figure 11. Vibrational energy distributions, $P(E)$, for Ph^- at (a) 300 K, (b) 500 K, (c) 690 K, and (d) 1000 K, calculated as described in the text. Filled symbols correspond to the binned populations within the E = 0–0.7 eV interval. The red solid curves represent the corresponding extrapolations for $E > 0.7$ eV interval using $g(E) \propto E^{n^*-1}$, with $n^* = 9.5$.

Figure 12

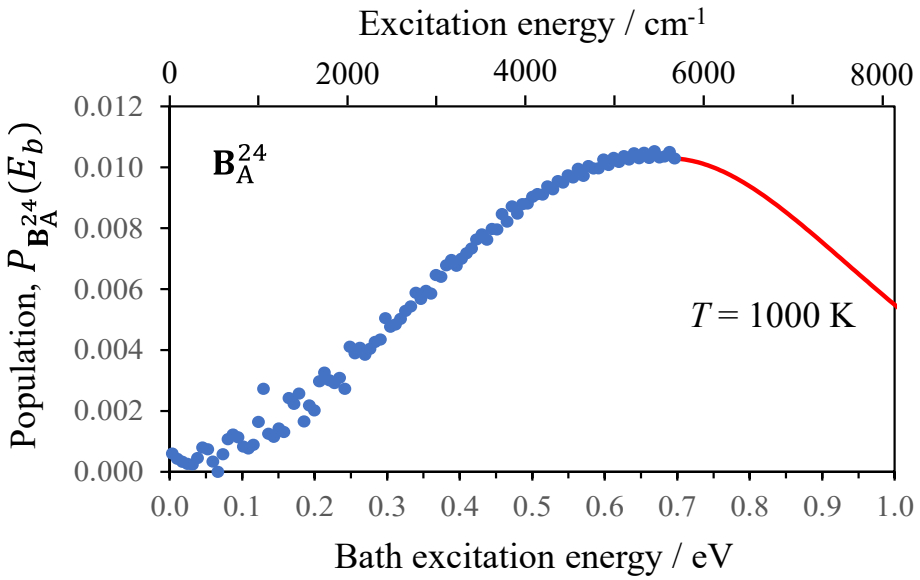

Figure 12. The vibrational energy distribution for the $\mathbf{B}_\mathrm{A}^{24}$ bath space, $P_{\mathbf{B}_\mathrm{A}^{24}}(E_b)$, at T = 1000 K, calculated as described in the text. Filled symbols correspond to the binned populations within the E_b = 0–0.7 eV interval. The red solid curve is an extrapolation using the DOS function $g_{\mathbf{B}_\mathrm{A}^{24}}(E_b) \propto E_b^{n^*-1}$ with n^* = 9.0 for E_b > 0.7 eV.

Figure 13

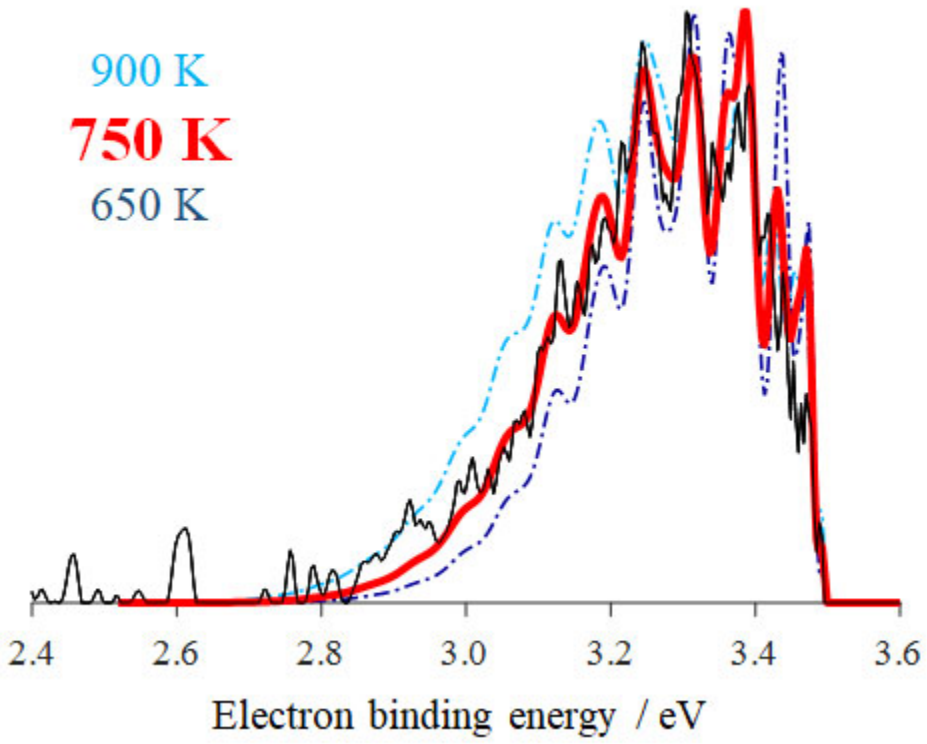

Figure 13. The bright-bath model applied to band A. The model spectra were calculated for the $\mathbf{Q}_A^3$ space (run A2) coupled to the bright $\mathbf{B}_A^{24}$ bath at three different temperatures, as indicated. Black: the experimental A band at 355 nm expanded from Figure 3a.

Figure 14

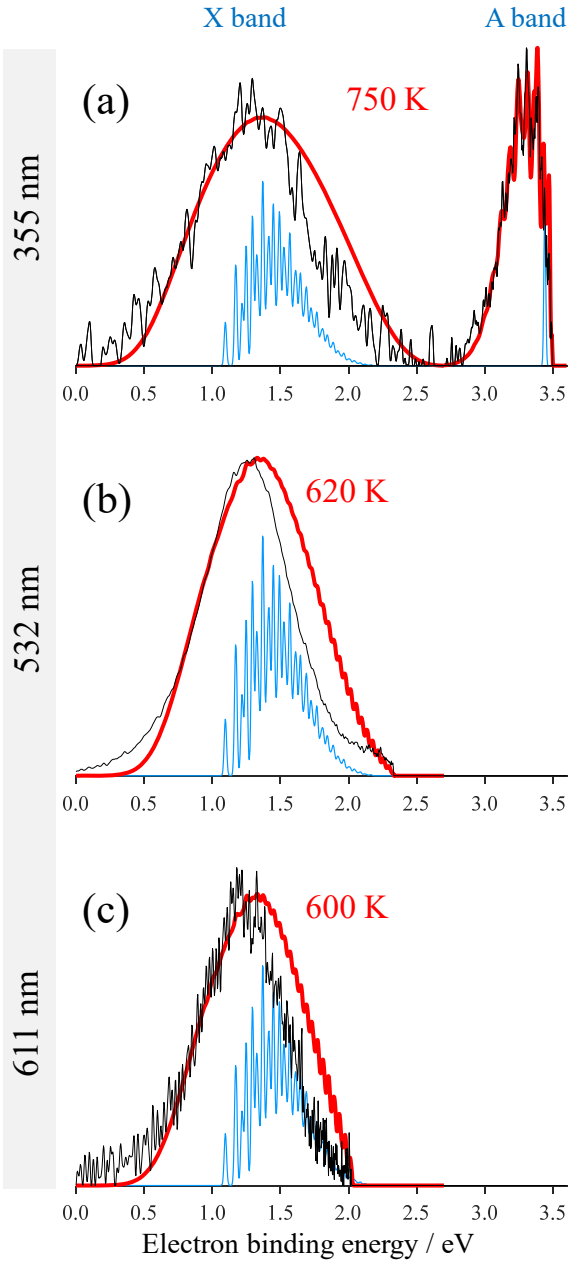

Figure 14. The bright-bath model applied to bands X and A at (a) 355 nm, (b) 532 nm, and (c) 611 nm. Red: model spectra calculated at the indicated temperatures within the $\mathbf{Q}_{\mathrm{X}}^{3}$ and $\mathbf{Q}_{\mathrm{A}}^{3}$ spaces (runs X5 and A2, respectively), coupled to the respective "bright" baths, $\mathbf{B}_{\mathrm{X}}^{24}$ or $\mathbf{B}_{\mathrm{A}}^{24}$. Modeling details are provided in the text. Light blue: $T = 0$ all-modes FC reference spectra calculated as described in Section 5.2 (runs X3 and A1). Black: the corresponding experimental spectra reproduced for comparison from Figure 3a-c.

Figure 15

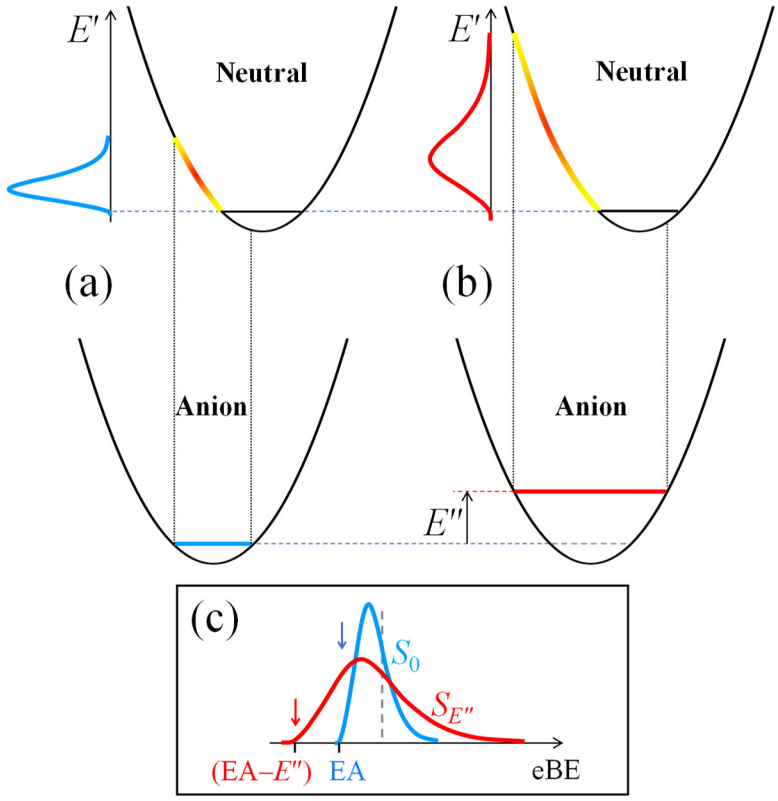

Figure 15. Spectral model based on the conservation of energy. Parts (a) and (b) compare the transitions from the ground (blue) and excited (red) vibrational states of the anion, respectively. The corresponding parts of the neutral potential accessed in the photodetachment are highlighted with a color gradient. To the left of each neutral potential are the schematic depictions of the expected spectral bands, $S_0(E')$ and $S_{E''}(E')$, respectively. (c) The spectral bands from (a) and (b) plotted together with respect to eBE. In the energy conservation model, the S_0(eBE) → $S_{E''}$(eBE) transform assumes an anchor point to right of the transition's VDE, shown schematically by the vertical dashed line. The transform is defined to shift the band's onset from eBE = EA in S_0(eBE) to eBE = EA – E'' in $S_{E''}$(eBE), while keeping the anchor unchanged. [Envision the blue curve representing S_0 as an elastic object anchored at the dashed line. Imagine pulling the left end of this object from its initial position at eBE = EA to eBE = EA – E'', while preserving the spectrum normalization, until the entire blue curve transforms into the red, for $S_{E''}$.]

Figure 16

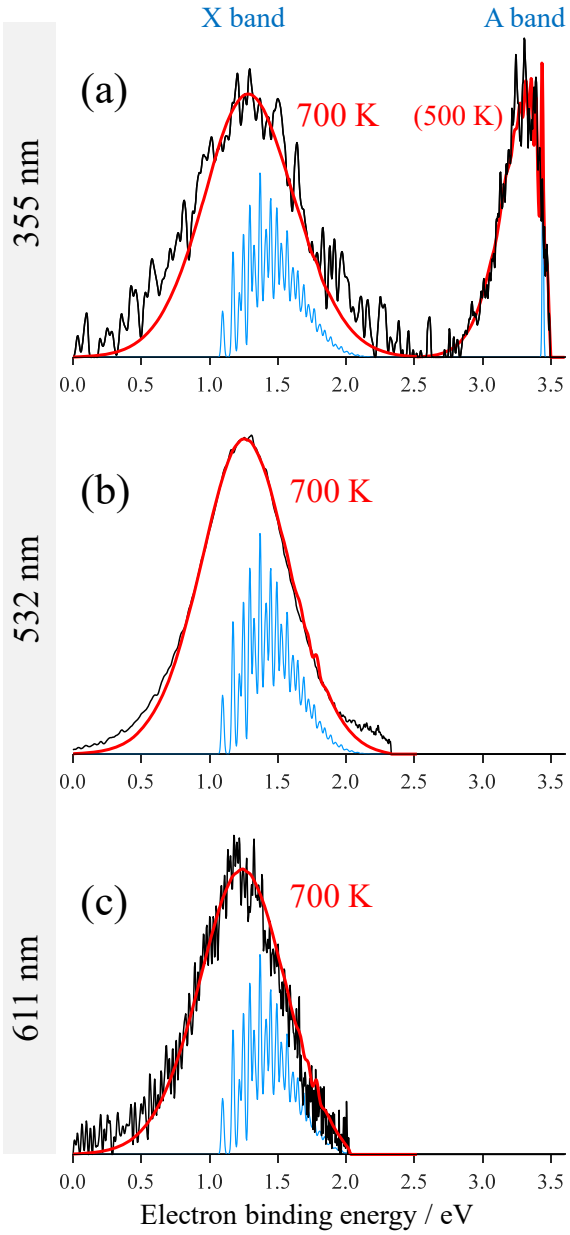

Figure 16. The energy-conservation model applied to bands X and A at (a) 355 nm, (b) 532 nm, and (c) 611 nm. Red: model spectra calculated at the indicated temperatures. Model details are provided in the text. Light blue: $T = 0$ all-modes FC reference spectra calculated as described in Section 5.2 (runs X3 and A1). Black: the corresponding experimental spectra reproduced for comparison from Figure 3a-c.

TOC graphic